Chapter 22
Airborne Wind Energy Conversion Using a Rotating Reel System

Pierre Benhaïem and Roland Schmehl

Abstract The study proposes a new airborne wind energy system based on the carousel concept. It comprises a rotary ring kite and a ground-based rotating reel conversion system. The moment generated by the ring kite is transferred by several peripheral tethers that connect to winch modules that are mounted on the ground rotor. A generator is coupled to this rotor for direct electricity generation. Because the ring kite is inclined with respect to the ground-rotor the length of the peripheral tethers has to be adjusted continuously during operation. The proposed system is designed to minimize the used land and space. This first study describes the fundamental working principles, results of a small-scale experimental test, a kinematic analysis of steady-state operation of the system and a power transmission analysis. Design choices for the ring kite are discussed, a strategy for launching and landing and methods for passive and active control are described.

22.1 Introduction

The potential of airborne wind energy conversion has been investigated by early explorative research [17, 20, 26] and confirmed by a larger number of recent theoretical and experimental studies [5, 6, 25, 27, 31]. It is however also clear that despite of the advantages of reduced material consumption, access to a larger wind resource and higher yield per installed system, the system-inherent use of a flexible tether requires a comparatively large surface area [9]. This contrasts the general

Pierre Benhaïem (✉)
7 Lotissement des Terres Blanches, 10160 Paisy-Cosdon, France
e-mail: pierre-benhaiem@orange.fr

Roland Schmehl
Delft University of Technology, Faculty of Aerospace Engineering, Kluyverweg 1, 2629 HS Delft, The Netherlands

motivation for designing an economically competitive wind energy that sweeps the whole frontal airspace, using less land and airspace.

Several concepts have been proposed to maximize the land use efficiency. For single kite systems operating on single ground stations the surface density can be increased by optimizing the spacial arrangement and operation of the systems while accounting for sufficient safety margins to avoid hazardous mechanical or aerodynamic interactions. The next conceptual improvement leads towards systems that operate multiple wings on a single ground stations [15]. For such systems the useful swept area can reach the occupied swept area, however, the technical complexity of such systems also increases significantly. Alternatively, single kite systems operating on single ground stations can be upscaled to increase the land use efficiency [15]. Finally, the complexity of the ground conversion can be increased, for example, using a large rotating structure (carousel) driven by several kites [14] or, alternatively, using carts that are pulled by kites on a round track [1, 2].

The present study proposes a new airborne wind energy system, the Rotating Reel Parotor (RRP), which combines a rotary ring kite with a ground-based rotating reel conversion system [8]. The concept has also been presented at the Airborne Wind Energy Conference 2015 [10]. Other airborne wind energy systems involving rotary kites are the "Gyromill" [23, 25], presented also in Chap. 23 of this book, which is based on onboard electricity generation, and the "Daisy Stack" [24], presented also in Chap. 21, which is transmitting shaft power to the ground, as the present concept. A related technology in the field of aviation is the tethered gyrocopter. In Sect. 22.2 the components of the system and their functions are described while Sect. 22.3 details the fundamental working principles. In Sect. 22.4 a small-scale model is presented and experimental results are discussed. In Sects. 22.6 and 22.5 the kinematics of the system and the torque transmission characteristics are investigated. Section 22.7 elaborates on ongoing and future investigations and Sect. 22.8 presents the conclusions of this study.

22.2 System Design

A conceptual sketch of the ground-based part of the system is illustrated in Fig. 22.1. Similar carousel-type configurations have been proposed for airborne wind energy

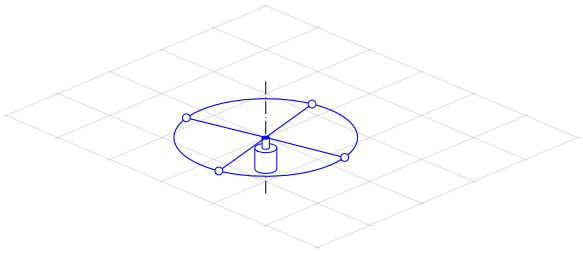

Fig. 22.1 The ground-based horizontal ring and its vertical axis of rotation. For direct conversion of the rotational motion a generator is coupled to the ring. The winch modules for the traction tethers are mounted on the ring and are indicated by circles

conversion [1, 14]. To convert the rotational motion of the ring structure directly into electricity it can be coupled to a generator using a gear mechanism. The peripheral traction tethers (not depicted) which drive the rotational motion of the ring are deployed from winch modules that are mounted at equidistant intervals along the ring. Each winch module comprises a cable drum with a connected generator that can also be used in motor mode.

A conceptual sketch of the rotary ring kite, denoted as Parotor, is illustrated in Fig. 22.2. The flying rotor is represented as an actuator ring which defines the swept

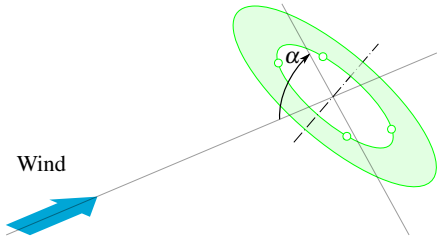

Fig. 22.2 The flying rotor is represented as actuator ring which is inclined to the flow by an angle α, its axis of rotation tilted downwind from the vertical axis by the same angle (for simplicity a sideslip angle β_s is not included here)

area of the physical rotor. A possible implementation of a small-scale model for test purposes will be discussed in Sect. 22.4.1. The flying rotor has a size that is about the size of the ground rotor and it is inclined with respect to the wind by an angle α. This inclination angle, also denoted as angle of attack, is identical to the angle between the axes of rotation of the ground and flying rotors.

Figure 22.3 shows how the flying rotor is connected to the ground rotor by peripheral tethers. Because the axes of rotation of the two rotors are not aligned the geometric distance between the ground and flying rotor attachment points changes continuously during rotation. As consequence the length of the connecting traction tethers needs to be adjusted continuously. This is the function of the ring-mounted

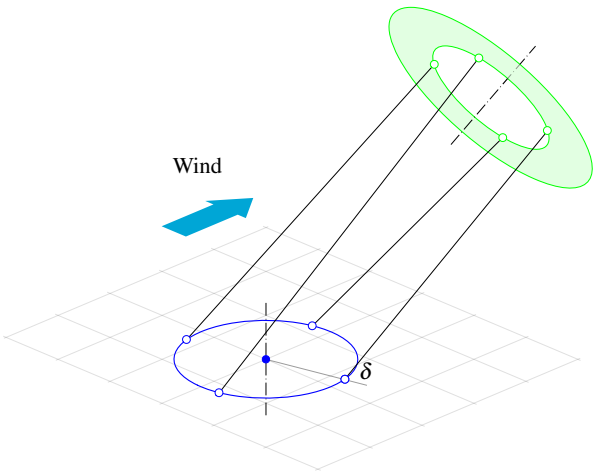

Fig. 22.3 The assembled Rotating Reel Parotor (RRP) in flight, just before operation. The tether attachment points at the flying rotor are indicated by circles. The radial line from the center of the ground rotor to one of the tether attachment points is an illustration element indicating the phase lag δ of the ground rotor. Before transmitting a torque the phase lag of the ground rotor is zero. The axis of rotation of the ground rotor is always vertical

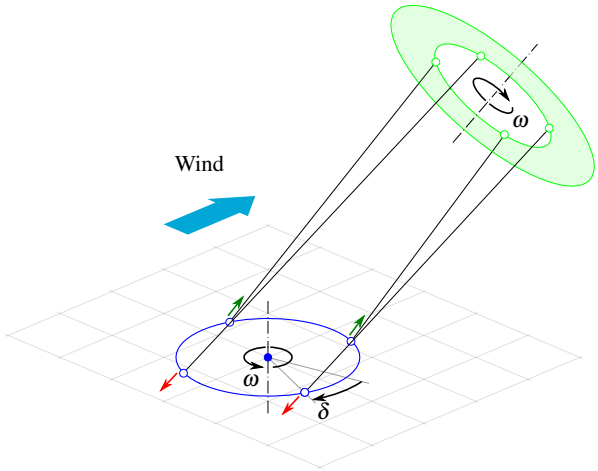

Fig. 22.4 The RRP system in operation with an angular speed ω and a phase lag angle $\delta = 35°$. The arrows at the winch modules indicate whether the corresponding tether is reeled out and energy is generated (green) or reeled in and energy is consumed (red). This definition implies that the reeling motion is relative to the winch modules which move on a circular path around the center of the ground rotor

winch modules shown in Figs. 22.1 and 22.3. When the geometric distance between two attachment points of a tether is increasing the corresponding winch module functions as a generator. When the distance is decreasing in the second half of the revolution, the winch is retracting the tether and is consuming energy. Figure 22.4 illustrates the Rotating Reel Parotor in operation. The flying rotor and the ground rotor are co-rotating at identical angular speeds, however, the driven ground rotor lags the flying rotor in phase.

A system of additional suspension lines can be added to support the flying rotor from the center of the ground rotor. Three different options are illustrated in Fig. 22.5, using lines or line segments of constant length. When in tension, all three implementations enforce a constant distance between the centers of the two rotors.

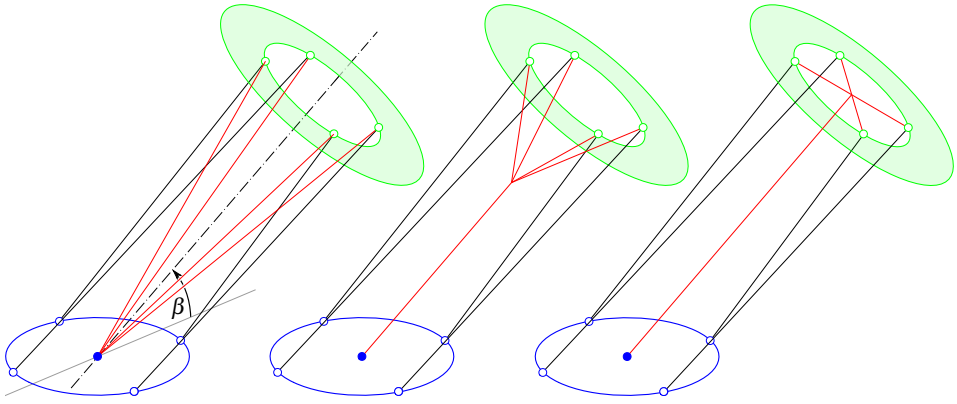

(a) Full tilt support (b) Strong tilt support (c) No tilt support

Fig. 22.5 Implementation options for suspension lines (in red) to support the flying rotor

The variant sketched in Fig. 22.5(a) additionally enforces a kinematic coupling between the orientation of the flying rotor, quantified by its angle of attack α and sideslip angle β_s, and the position of the rotor, quantified by the ground elevation angle β and azimuth angle ϕ of the rotor center point. Although this constraint could be a way to stabilize the operation of the system, the additional lines increase the losses due to aerodynamic drag. The bridle-type variant sketched in Fig. 22.5(b) reduces the drag losses and and allows for some tilt motion of the rotor while the central line variant sketched in Fig. 22.5(c) has no additional drag losses and does not impose any constraint on the tilt motion. It should be noted that the suspension lines for the flying rotor can alternatively be attached to an additional lifting kite.

22.3 Working Principles

A general feature of airborne wind energy is the use of flying devices to extract kinetic energy from the wind and to transfer it as either mechanical or electrical energy to the ground, using flexible tethers. Because flexible tethers can only transfer tensile forces an additional mechanism is required on the ground to convert the traction power into shaft power, which can be converted by electrical generators.

22.3.1 Power Transfer and Power Takeoff

The proposed concept employs a set of peripheral tethers to transfer the rotational motion of a flying rotor to a ground rotor. This tensile torque transmission system makes use of the tangential components of the tether forces acting on the ground rotor. The function of the normal force components is to keep the transmission system in tension, which is an obvious prerequisite for the functioning of the system.

It is important to note that the transmission of torque implies torsion of the tether system. As can be seen in Fig. 22.4 the angle of twist, which is identical to the phase lag angle δ of the ground rotor, determines how the tether force is decomposed into tangential and normal components. At small to moderate values of the twist angle, an increasing torsion reduces the angle at which the tethers attach to the ground rotor. This geometric effect increases the tangential components and it allows the tether system to adjust to variations of the torque which can occur, for example, as a result of a fluctuating wind speed. At larger values of the twist angle, for $\delta > 90^\circ$, the effect decreases because the tether system increasingly constricts in a point on the axis of rotation. At $\delta = 180^\circ$ the tether system reaches the singular condition at which all tethers intersect in one point and no practically relevant torque can be transmitted.

The transmission characteristics are also influenced by the distance between the two rotors in relation to their diameter. The further the rotors are apart the smaller the tangential components of the tether forces, the less effective the above mentioned

coupling effect between torsion and torque and the lower the torsion stiffness of the tether system. If the rotors are many diameters apart the tether system can not be used effectively for torque transmission.

It can be concluded that on the level of the individual tethers the torsion stiffness of the system is caused by tensile forces, the rotational motion generated by circular traction of the ground rotor. Because the axis of rotation of the flying rotor is tilted downwind the rotational motion requires that the tether lengths are adjusted continuously to the varying geometric distances between the attachment points. As described in Sect. 22.2 this is the function of the winch modules on the ground rotor which compensate the distance variations by reeling the tethers in and out. The two fundamental modes of energy generation are discussed in the following.

22.3.2 Direct Mode of Energy Generation

In this mode the rotational motion of the ground rotor is converted directly into electricity, using one or more generators that are coupled to the rotor by a gear mechanism, as illustrated schematically in Fig. 22.1. The winch modules manage the kinematically induced length variation of the peripheral tethers, as shown in Fig. 22.4. They are controlled in such a way that the tension in the tethers is equal and constant during operation. The modules are electrically interconnected such that the generated and consumed energy is balanced, avoiding the implementation of expensive temporary energy storage. To account for losses in the electrical machines a small amount of electricity is provided by the main generator which is driven directly by the rotor.

By adding suspension lines, as shown in Fig. 22.5, the force level in the system of peripheral tethers is lowered and, as consequence, also the generated and consumed amounts of energy. Because of the reduced losses in the electrical machines the total amount of electrical energy required for the actuation of the tether system is decreased. However, with the addition of suspension lines the tensile torque transmission system becomes more complex and in particular also statically indeterminate (hyperstatic). As consequence this poses additional challenges to the control systems of the winch modules.

22.3.3 Secondary Mode of Energy Generation

In this mode the length variation of the peripheral tethers is converted into electricity, using the winch modules on the ground rotor alternatingly as generators and motors. The suspension lines are essential and are used to selectively reduce the tether tension during reel-in. As consequence, the winch modules consume less energy during reel-in than they generate during reel-out, resulting in a positive net energy of the phase-shifted interconnected modules. The proposed technique is illustrated

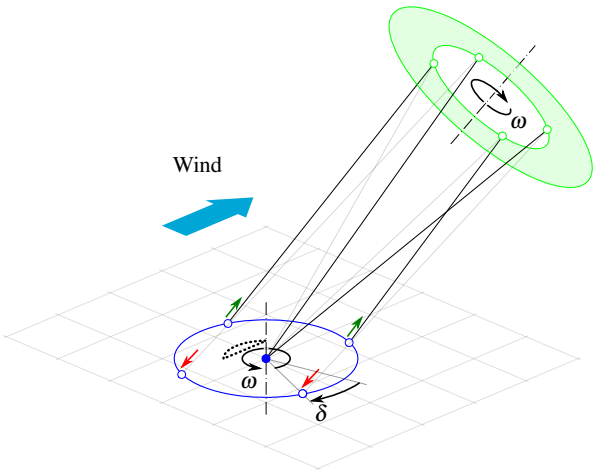

Fig. 22.6 The secondary mode of energy generation with two tensioned tethers and two tensioned suspension lines highlighted. Unloaded tensile components are hinted. The two winch modules producing electricity are next to the green arrows, pointing away from the modules, while the two winch modules reeling the tethers in are next to the red arrows, pointing towards the modules. The doted loop is the ground track of the resultant tensile force in the system assuming perfect unloading during reel-in

schematically in Fig. 22.6. The two winch modules in reel-out mode operate on tensioned tethers while the two winch modules in reel-in mode operate on untensioned tethers. The shift from tensioned reel-out to untensioned reel-in is managed by the force control of the winch modules. When switching from reel-out to reel-in the set value of the tether force is decreased from its nominal value to a low value. As consequence, the tensile load shifts from the peripheral tether to the corresponding suspension line which inevitably affects the static force balance and geometry of the entire torque transmission system. Accordingly, the set value of the tether force is increased back to the nominal value when switching to reel-out and the tensile load shifts from the suspension line back to the peripheral tether.

Because of the induced rotational asymmetry of the force transmission the resultant force acting on the ground rotor does not pass through a constant point on the ground plane anymore, as it does for the direct mode of energy generation. The resultant tensile force in the transmission system is essentially unsteady and tracks a periodic loop on the ground plane which is shifted sideways towards the half of the ground rotor that moves against the wind. This is indicated as dotted line in Fig. 22.6. The rotational asymmetry affects also the flying rotor which inevitably performs a tumbling motion. In particular the switching of the force transfer, which, in the illustrated example affects two winch modules at the same time, introduces a strong discontinuity in the transmission system. In practice, the switching needs to be replaced by a sufficiently smooth process to avoid a periodic jolting of the entire system.

22.3.4 Discussion

The direct and secondary modes of energy generation differ only in the force control strategy implemented for winch modules. Because of this, the two modes can in principle be blended by the control algorithm. However, because of its rotational asymmetry and unsteadyness it is still an open question whether the secondary mode has any practical relevance.

22.4 Experimental Tests of a Small-Scale Model

A physical model of the proposed RRP system has been designed and built at small scale. Initial tests have been performed to demonstrate the fundamental working principles and to provide an initial assessment of the transmitted torque.

22.4.1 Test Setup

The small-scale model is shown in operation in Fig. 22.7 and the parameters of the test setup are summarized in Table 22.1. The geometric proportions and the elevation angle are roughly the same as for the intermediate-scale system described in Sect. 22.6.5. In place of the winch modules that a larger production system would

Fig. 22.7 Small-scale system built with two spars, a ring, four retractable leashes, a rotating tray, a parachute kite and semi-rigid rotor blades. The system uses four peripheral tethers and several suspension lines. The flying rotor measures 1.3 m from tip to tip

Table 22.1 Design and operational parameters of the small-scale system. Because of the close proximity of the flying rotor to the ground (about 1 m) it was exposed to significant turbulent fluctuations of the wind velocity. The setup uses suspension lines

Parameter name	Symbol	Value	Unit
Average wind speed	$\bar{v}_\mathrm{w}$	6.0	m/s
Ground rotor diameter	d_g	0.8	m
Flying rotor inner diameter	d_k	0.6	m
Flying rotor outer diameter	$d_\mathrm{k,o}$	1.3	m
Number of rotor blades	b	8	
Blade span		0.35	m
Blade root chord		0.12	m
Blade tip chord		0.04	m
Flying rotor swept area	S	1.0	m^2
Lifting kite area		2.0	m^2
Number of peripheral tethers	N	4	
Tether length, minimum	$l_\mathrm{t,min}$	0.8	m
Tether length, maximum	$l_\mathrm{t,max}$	1.4	m
Tether length lifting kite		10	m
Elevation angle kite center	β	40	deg

use, this technology demonstrator has off-the-shelf retractable leashes mounted on the ground rotor. As they are equipped with a rotational spring mechanism, these leashes do not produce a constant force but one that is linearly increasing with the deployed tether length. This is an important aspect for the interpretation of the results and the comparison with the analytical calculations and numerical simulations in the following sections. For standalone testing of the rotating reel conversion system the ring kite is replaced by a top ring which is rotated by hand. To assess the torque transmission characteristics the torque imposed on the top ring, τ_k, and the torque arriving at the ground rotor, τ_g, are measured with two torque meters. These tests showed that the torque transmission coefficient is about $\tau_\mathrm{g}/\tau_\mathrm{k} = 0.5$.

The design challenge of this small-scale test setup was the matching of the torques generated by the ring kite and converted by the described rotating reel conversion system. The baseline design of the ring kite shown in Fig. 22.7 uses eight semi-rigid rotor blades. To operate this kite at wind speeds between 5 to 6 m/s a sled kite was added to provide additional lift. With active conversion system a rotational speed of one revolution per second has been obtained for short times. This relatively high value is due to the small dimensions of the technology demonstrator. The rotor with 8 blades has a high solidity, so a low efficiency compared to the Betz limit [16]. However, the generated torque was appropriate for the tests. A rotor with 16 blades has also been tested and, as expected, produced a higher torque, while achieving lower angular speeds. More complete test data is provided in Sect. 22.4.2.

As concluded in Sect. 22.3.1 the rotating reel conversion system works only if the tethers are not too long compared to the inner diameter of the ring kite. This diameter is indeed approximately equal to the tip height of the system, as shown in Sect. 22.6. Because the wind is generally stronger at higher altitudes [3] the RRP system will have to be quite large. However, the implementation of a mo-

torized ground rotor could be studied for the purpose of increasing the transmitted torque with longer tethers and for applying the second mode of energy generation, as described in Sect. 22.3.3. Such a motorized ground rotor could also be used for launching.

22.4.2 Experimental Results

The objective of the experimental tests has been to demonstrate the fundamental working principles and to quantitatively assess the effectiveness of the energy conversion mechanisms. As none of the elements was optimized the coefficient of the transmitted power cannot be directly deduced. Because the test setup does not include a central generator the achievable direct power takeoff of the ground rotor is assessed by the power that is required to overcome the internal friction torque of the central swiveling tray. Because the test setup uses retractable leashes instead of controlled winch modules, the energy budget related to the tether actuation is assessed on the basis of the stored potential energy of the leashes. The test results for the setup defined in Table 22.1 are summarized in Table 22.2. The limiting values $\omega_{\min}$

Table 22.2 Measured properties of the small-scale system

Parameter name	Symbol	Value	Unit
Angular speed, minimum	$\omega_{\min}$	2	rad/s
Angular speed, maximum	$\omega_{\max}$	6	rad/s
Angular speed, average	$\overline{\omega}$	3	rad/s
Angular speed, freewheel[a]	$\omega_{\tau=0}$	12	rad/s
Tip speed ratio, minimum	$\lambda_{\min}$	0.216	
Tip speed ratio, maximum	$\lambda_{\max}$	0.648	
Tip speed ratio, average	$\overline{\lambda}$	0.324	
Tip speed ratio, freewheel[a]	$\lambda_{\tau=0}$	1.3	
Tether force, minimum	$F_{\mathrm{t,min}}$	0.88	N
Tether force, maximum	$F_{\mathrm{t,max}}$	1.76	N
Tether reeling power, average	$\overline{P}_{\mathrm{reel}}$	1.5	W
Friction torque central swivel	τ_{μ}	0.225	Nm
Friction power central swivel	P_{μ}	0.675	W
Flying rotor power, Betz limit	$P_{\max}$	35	W

[a] peripheral tethers detached

and $\omega_{\max}$ describe the range of measured angular speeds of the system, $\overline{\omega}$ a representative average value. The value $\omega_{\tau=0}$ is achieved without conversion system, using only suspension lines. Similarly the values $\lambda_{\min}$ and $\lambda_{\max}$ describe the range of measured tip speed ratios, $\overline{\lambda}$ a representative average and $\lambda_{\tau=0}$ the ratio without conversion system. $F_{\mathrm{t,min}}$ and $F_{\mathrm{t,max}}$ describe the limiting values of the tether forces that correspond with the tether lengths $l_{\mathrm{t,min}}$ and $l_{\mathrm{t,max}}$.

Assuming linear elastic behavior, the potential energy stored in the spring mechanism of the leash can be calculated as

$$E = \frac{1}{2}\left(F_{\mathrm{t,max}} + F_{\mathrm{t,min}}\right)\left(l_{\mathrm{t,max}} - l_{\mathrm{t,min}}\right). \tag{22.1}$$

The tether extends from $l_{\mathrm{t,min}}$ to $l_{\mathrm{t,max}}$ during half a revolution of the rotor which is associated with the time period

$$\Delta t = \frac{\pi}{\omega}. \tag{22.2}$$

Considering that two leashes of the system are continuously in reel-out mode we can derive the average equivalent power for these two leashes as

$$\overline{P}_{\mathrm{reel}} = 2\frac{E}{\Delta t} = \left(F_{\mathrm{t,max}} + F_{\mathrm{t,min}}\right)\left(l_{\mathrm{t,max}} - l_{\mathrm{t,min}}\right)\frac{\omega}{\pi}. \tag{22.3}$$

Based on the numerical values in Tables 22.1 and 22.2, and using the average value of the angular speed, we can calculate the value of $\overline{P}_{\mathrm{reel}}$ specified in Table 22.2. The friction torque τ_μ of the central swivel was measured at the average angular speed and using this value we can calculate the value of the friction power P_μ listed in Table 22.2.

The power values P_μ and $\overline{P}_{\mathrm{reel}}$ provide a first insight into the energy budget of the proposed concept. Assuming that the friction in the swivel can be reduced substantially, a power in the order of P_μ would be available for direct continuous conversion into electricity. In contrast to this, the potential energy E quantified by Eq. (22.1) is cyclically progressing through the spring mechanisms of the leashes but in balance for the entire system. This potential is only accessible when using suspension lines to selectively reduce the tether tension during reel-in, however, this was not possible in this simple test setup. As a general conclusion it should be noted that an extrapolation of these values to larger systems is critical if not questionable because of the small scale and the significant measurement uncertainties in this setup.

The efficiency of the flying rotor was not measured, but as it uses numerous semi-rigid blades forming a high-solidity rotor the efficiency is considered to be far below the value of the Betz limit. Defining the wind power density as

$$P_{\mathrm{w}} = \frac{1}{2}\rho v_{\mathrm{w}}^3, \tag{22.4}$$

this limiting power value can be computed as

$$P_{\mathrm{max}} = P_{\mathrm{w}} S \frac{16}{27}\cos^3\beta, \tag{22.5}$$

where the factor $\cos^3\beta$ accounts for the misalignment of the flying rotor with respect to the wind [13, p. 98]. By inserting the applicable numerical values we can calculate the value listed in Table 22.2.

The initial tests have shown the potential but also the challenges of the concept. Indeed there have been jolts during rotation of the system and the tests indicated

that the turbulent fluctuations of the wind at close proximity to the ground was a possible cause of these jolts. Another contribution is due to the use of retractable leashes with spring mechanisms. The inevitable force variations during rotation induce a tumbling motion of the flying rotor, which becomes stronger with decreasing elevation angle.

Following the initial tests, the effect of parameter and design variations has been studied. Firstly, leashes with lower tensile strength were used. While the baseline design used leashes which generated a force of 1.91 N for 1.30 m of reeled out tether, these generated the same force with 2.20 m of reeled out tether. Secondly, the tensile strength was increased by pairing leashes such that each pair of leashes generated a force if 1.91 N with 0.82 m of reeled out tether. These tests indicated that the tensile strength must be sufficiently high to avoid excessive twist of the tether system and eventually entangling of the tethers. On the other hand if the tensile strength is to high the tether system can not transfer the torque required for a continuous rotation. A larger Rotating Reeling Parotor system of about 5 m diameter would allow harnessing better wind at a height of 5 m.

To address the problem of turbulent wind fluctuations and their effect on the reproducibility of results a leaf blower was used to produce a constant airflow. The center of the ring kite was suspended in space by means of a bar. The modified design and test setup is summarized in Table 22.3. Parameters that are not listed

Table 22.3 Design and operational parameters for the modified design with 16 rotor blades and an increased flow velocity. To increase the tensile strength leashes are arranged in pairs. The setup does not use suspension lines

Parameter name	Symbol	Value	Unit
Number of rotor blades	b	16	
Elevation angle kite center	β	65	deg
Number of peripheral tethers	N	4	
Tether length, minimum	$l_{\mathrm{t,min}}$	0.20	m
Tether length, maximum	$l_{\mathrm{t,max}}$	0.62	m
Tether force, average	$\overline{F}_{\mathrm{t}}$	0.91	N
Angular speed	ω	5	rad/s
Angular speed, freewheel[a]	$\omega_{\tau=0}$	9	rad/s
Tether reeling power, average	$\overline{P}_{\mathrm{reel}}$	1.16	W

[a] peripheral tethers detached and suspension lines added

have not been modified from the baseline design summarized in Table 22.1. The average tether force is calculated as

$$\overline{F}_{\mathrm{t}} = \frac{1}{2}\left(F_{\mathrm{t,max}} - F_{\mathrm{t,min}}\right) \tag{22.6}$$

In these tests it was possible to operate the RRP system in a steady state rotation without jolts and generating some power. It is envisioned that more thorough results including the torque transmission efficiency as a function of the elevation angle can be achieved using a wind tunnel.

22.5 Kinematics of Steady-State Operation

The revolving system of peripheral tethers has the double function of anchoring the rotary ring kite to the ground and transferring the generated aerodynamic moment to the ground-based conversion system. Uncommon for airborne wind energy systems, the combination of these two functions entails comparatively complex tether kinematics which is governed by strong nonlinear coupling effects. In this section a kinematic model for the steady-state operation of the tensile torque transmission system is derived. This model is used to formulate analytical expressions for the instantaneous tether length and rotor attachment angles which are the starting base for the analysis of the power transmission characteristics in the following section.

22.5.1 Steady-State Operation as an Idealized Condition

The distinguishing feature of the ring kite is that it employs the effect of autorotation to convert kinetic energy from the wind into aerodynamic lift and usable shaft power. To analyze the steady-state flight of this kite the spinning rotor is represented as a non-spinning planar actuator ring. This abstraction, which hides the implementation details of the physical rotor, is shown in Fig. 22.8. The orientation of the actuator ring with respect to the flow is described by the sideslip angle β_s and the angle of attack α. The actuator ring is regarded as a flying object with three translational and two rotational degrees of freedom. The two rotational degrees of freedom of the actuator ring, roll and pitch, tilt the spinning axis of the rotor. The aerodynamic lift

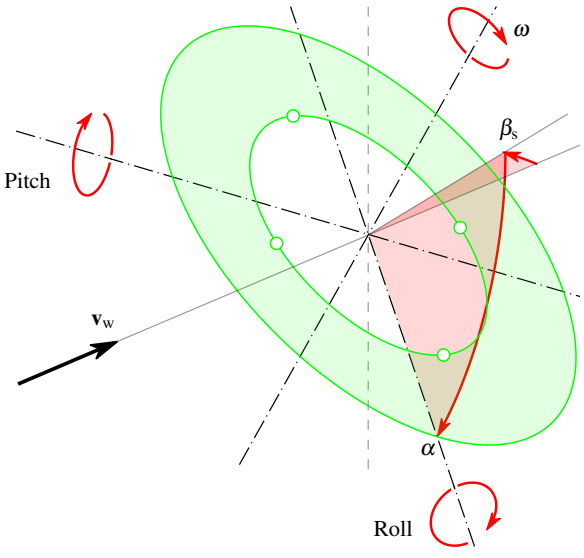

Fig. 22.8 The actuator ring model of the rotary ring kite. The inclination of the ring with respect to the flow is described by two successive rotations. The sideslip angle β_s describes the rotation around the vertical axis while the angle of attack α describes the rotation of the ring around its pitch axis. Roll and pitch axes are attached to the actuator ring and not to the physical rotor. The angular speed ω of the rotor is an operational parameter which, next to the flow angles β_s and α, affects the aerodynamic lift and drag of the ring

L and drag D of the actuator ring are functions of the sideslip angle β_s, the angle of attack α, the angular speed ω, the physical dimensions of the rotor and the wind speed v_w.

The objective of the study is to add a system of actuated peripheral tethers, as outlined in Sect. 22.2, to constrain the degrees of freedom of the ring kite to a steady flight state at a constant position with a constant axis of rotation. However, although the length of the tethers is adjusted continuously to the required geometrical distance, the tether attachment angles at the rotors vary periodically with the rotation angle. Caused by the rotational asymmetry of the tilted tether system, the directional variations of the tether forces lead to transverse resultant forces that induce periodic compensating motions of the flying rotor.

For the purpose of the kinematic analysis these compensating motions are neglected, assuming an idealized condition of steady-state operation in which the ring kite has a constant position with a constant axis of rotation. By prescribing this condition, the length of the individual tethers can be formulated as analytic functions of time and other relevant problem parameters. For the purpose of the analysis it is assumed that all tethers are inflexible and tensioned and can thus be represented as straight lines.

Figure 22.9 shows the configuration of the RRP system with four tethers and without any additional suspension lines. For simplicity we restrict the analysis to the case of steady-state operation of the ring kite with its center point K always in the $x_w z_w$-plane. In this particular case the azimuth angle ϕ vanishes at all times. When using additional suspension lines, as illustrated in Fig. 22.5, the distance l_K of the kite center point from the origin is constant and the axis of rotation of the ring kite has to pass through the origin O which the following kinematic constraints

$$\alpha = 90^\circ - \beta, \tag{22.7}$$

$$\beta_s = 0. \tag{22.8}$$

A and B denote a pair of representative tether attachment points at the flying rotor and the ground rotor, respectively. Because the angular speed ω of both rotors is assumed to be constant the rotation angle is given by ωt, adding a constant phase lag δ for the flying rotor. The tethers are attached on the ground rotor at a distance R_g from the center O, on the flying rotor at a distance R_k from the center K. The tips of the rotor blades are at a distance $R_{k,o}$ from the center K. The distance l_K between the centers of the two rotors is regarded as a parameter that is prescribed either as a distance constraint when using suspension lines, as shown in Fig. 22.5, or by the controlled actuation of the tether system.

22.5.2 Dimensionless Problem Parameters and Reference Frames

From the illustration of the steady-state operation of the system in Fig. 22.9 we can identify $\alpha, \beta_s, \beta, \delta, \omega t, R_g, R_k$ and l_K as the fundamental parameters of the kine-

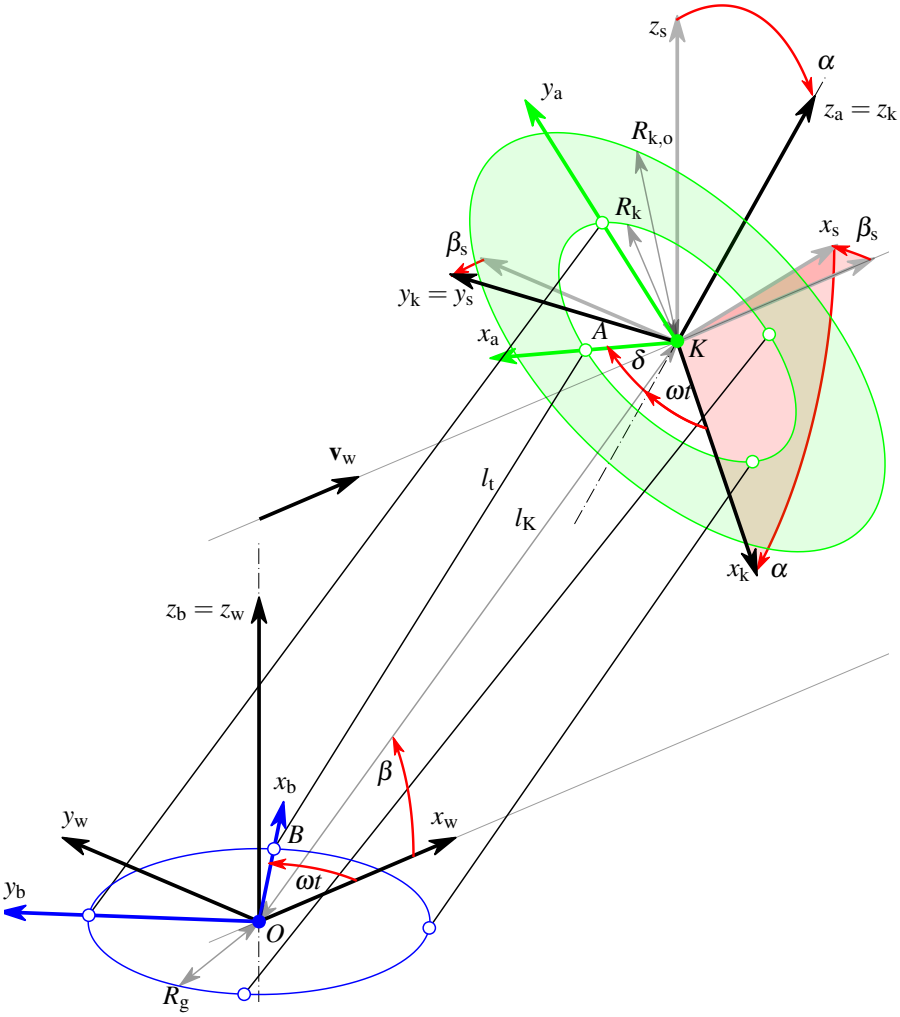

Fig. 22.9 Configuration of the RRP system with $N = 4$ revolving tethers for steady-state operation in the $x_w z_w$-plane ($\phi = 0$). The winch modules and the attachment points on the flying rotor are indicated by circles, A and B denote a representative pair and l_t denotes the length of the connecting tether. The distance of the kite center point K from the origin O is denoted as l_K. The ground rotor lags the flying rotor in phase by and angle δ

matic problem of steady-state operation with the kite center restricted to the $x_w z_w$-plane ($\phi = 0$). The corresponding set of dimensionless parameters are the angles $\alpha, \beta_s, \beta, \delta$ and ωt together with the geometric ratios R_g/R_k and l_K/R_k.

Included in Fig. 22.9 are the right-handed Cartesian reference frames which are used to describe the relative positions on the two rotors. The wind reference frame (x_w, y_w, zw) is considered to be an inertial frame with origin O, its x_w-axis aligned with the wind velocity vector $\mathbf{v}_w$ and its z_w-axis pointing towards zenith. The ref-

erence frame (x_b, y_b, z_b) is attached to the ground rotor, with origin at O, its x_b-axis pointing towards the tether attachment point B and rotating with angular velocity ω around the z_w-axis.

The sideslip reference frame (x_s, y_s, z_s) has its origin at the kite center point K and is constructed from the wind reference frame by rotating the x_w- and y_w-axes by the sideslip angle β_s around the vertical axis. The kite reference frame (x_k, y_k, z_k) is constructed from the sideslip reference frame by rotating the x_s- and z_s-axes by the angle of attack α around the y_s-axis. Following a common aeronautical convention, the x_k- and y_k-axes coincide with the roll- and pitch-axes of the actuator ring, respectively. The reference frame (x_a, y_a, z_a) is attached to the flying rotor, with origin at K, its x_a-axis pointing towards the tether attachment point A and rotating with angular speed ω around the z_k-axis, leading the rotation of the ground rotor by an angle δ.

22.5.3 Kinematic Properties

In the following the kinematic relations for the two rotors are derived formulating the positions of points A and B as functions of the geometric and kinematic parameters of the steady-state problem. Point B is fixed to the ground rotor at radius R_g and its coordinates in the wind reference frame can be written as

$$\mathbf{r}_B = \begin{bmatrix} \cos(\omega t) \\ \sin(\omega t) \\ 0 \end{bmatrix} R_g. \tag{22.9}$$

The coordinates of the kite center point K are

$$\mathbf{r}_K = \begin{bmatrix} \cos\beta \\ 0 \\ \sin\beta \end{bmatrix} l_K. \tag{22.10}$$

Point A is fixed to the flying rotor at radius R_k. To determine its coordinates in the wind reference frame we first define the transformation matrices $\mathbf{T}_{ws}$ and $\mathbf{T}_{sk}$ which describe the individual rotations by angles β_s and α, respectively,

$$\mathbf{T}_{ws} = \begin{bmatrix} \cos\beta_s & -\sin\beta_s & 0 \\ \sin\beta_s & \cos\beta_s & 0 \\ 0 & 0 & 1 \end{bmatrix}, \qquad \mathbf{T}_{sk} = \begin{bmatrix} \cos\alpha & 0 & \sin\alpha \\ 0 & 1 & 0 \\ -\sin\alpha & 0 & \cos\alpha \end{bmatrix}.$$

Combining these by multiplication we can derive the matrix $\mathbf{T}_{wk}$ which describes the coordinate transformation from the kite reference frame to the wind reference frame by two successive rotations

$$\mathbf{T}_{\mathrm{wk}} = \mathbf{T}_{\mathrm{ws}}\mathbf{T}_{\mathrm{sk}} = \begin{bmatrix} \cos\beta_{\mathrm{s}}\cos\alpha & -\sin\beta_{\mathrm{s}} & \cos\beta_{\mathrm{s}}\sin\alpha \\ \sin\beta_{\mathrm{s}}\cos\alpha & \cos\beta_{\mathrm{s}} & \sin\beta_{\mathrm{s}}\sin\alpha \\ -\sin\alpha & 0 & \cos\alpha \end{bmatrix}. \tag{22.11}$$

Using this transformation matrix we can formulate the coordinates of point A in the wind reference frame as

$$\mathbf{r}_{\mathrm{A}} = \mathbf{T}_{\mathrm{wk}} \begin{bmatrix} \cos(\omega t+\delta) \\ \sin(\omega t+\delta) \\ 0 \end{bmatrix} R_{\mathrm{k}} + \begin{bmatrix} \cos\beta \\ 0 \\ \sin\beta \end{bmatrix} l_{\mathrm{K}}. \tag{22.12}$$

Defining the instantaneous distance vector pointing from point B to point A as

$$\mathbf{r}_{\mathrm{A}} - \mathbf{r}_{\mathrm{B}} = \begin{bmatrix} l_{\mathrm{t,x}} \\ l_{\mathrm{t,y}} \\ l_{\mathrm{t,z}} \end{bmatrix}, \tag{22.13}$$

the coordinates of this vector can be calculated as

$$\begin{aligned} \mathbf{r}_{\mathrm{A}} - \mathbf{r}_{\mathrm{B}} = & \begin{bmatrix} \cos\beta_{\mathrm{s}}\cos\alpha\cos(\omega t+\delta) - \sin\beta_{\mathrm{s}}\sin(\omega t+\delta) \\ \sin\beta_{\mathrm{s}}\cos\alpha\cos(\omega t+\delta) + \cos\beta_{\mathrm{s}}\sin(\omega t+\delta) \\ -\sin\alpha\cos(\omega t+\delta) \end{bmatrix} R_{\mathrm{k}} \\ & + \begin{bmatrix} \cos\beta \\ 0 \\ \sin\beta \end{bmatrix} l_{\mathrm{K}} - \begin{bmatrix} \cos(\omega t) \\ \sin(\omega t) \\ 0 \end{bmatrix} R_{\mathrm{g}}, \end{aligned} \tag{22.14}$$

and used to determine the geometric distance as

$$l_{\mathrm{t}} = |\mathbf{r}_{\mathrm{A}} - \mathbf{r}_{\mathrm{B}}| = \sqrt{l_{\mathrm{t,x}}^2 + l_{\mathrm{t,y}}^2 + l_{\mathrm{t,z}}^2}. \tag{22.15}$$

Following the convention used in Sect. 22.5.2 the dimensionless tether length is defined as $l_{\mathrm{t}}/R_{\mathrm{k}}$.

To derive the tether reeling velocity as the rate of change of tether length, $v_{\mathrm{t}} = dl_{\mathrm{t}}/dt$, we apply the general differentiation rule

$$\frac{d}{dt}\sqrt{\mathbf{r}\cdot\mathbf{r}} = \frac{\mathbf{r}}{\sqrt{\mathbf{r}\cdot\mathbf{r}}}\cdot\frac{d\mathbf{r}}{dt}, \tag{22.16}$$

to Eq. (22.15) to get

$$v_{\mathrm{t}} = \frac{1}{l_{\mathrm{t}}}\left(l_{\mathrm{t,x}}\frac{dl_{\mathrm{t,x}}}{dt} + l_{\mathrm{t,y}}\frac{dl_{\mathrm{t,y}}}{dt} + l_{\mathrm{t,z}}\frac{dl_{\mathrm{t,z}}}{dt}\right). \tag{22.17}$$

The individual coordinate derivatives included in the right hand side of this equation are obtained by differentiating Eq. (22.14) as

$$\frac{d}{dt}(\mathbf{r}_\mathrm{A}-\mathbf{r}_\mathrm{B}) = \begin{bmatrix} -\cos\beta_\mathrm{s}\cos\alpha\sin(\omega t+\delta) - \sin\beta_\mathrm{s}\cos(\omega t+\delta) \\ -\sin\beta_\mathrm{s}\cos\alpha\sin(\omega t+\delta) + \cos\beta_\mathrm{s}\cos(\omega t+\delta) \\ \sin\alpha\sin(\omega t+\delta) \end{bmatrix} R_\mathrm{k}\omega - \begin{bmatrix} -\sin(\omega t) \\ \cos(\omega t) \\ 0 \end{bmatrix} R_\mathrm{g}\omega. \quad (22.18)$$

The dimensionless tether reeling velocity is defined as $v_\mathrm{t}/(\omega R_\mathrm{k})$.

Next to the tether length l_t and its rate of change v_t a third important derived kinematic property is the angle γ at which the tethers attach to the rotor rings. This angle controls the transfer of torque from the flying rotor to the tether system and further to the ground rotor. Considering the attachment of the tether to the ground rotor and defining the unit vectors pointing along the tether and from the origin to point B as

$$\mathbf{e}_\mathrm{t} = \frac{\mathbf{r}_\mathrm{A}-\mathbf{r}_\mathrm{B}}{l_\mathrm{t}}, \quad (22.19)$$

$$\mathbf{e}_\mathrm{x}^\mathrm{b} = \frac{\mathbf{r}_\mathrm{B}}{R_\mathrm{g}}, \quad (22.20)$$

the tether attachment angle γ_g can be computed from the z_w-component of the cross product of both vectors as

$$\cos\gamma_\mathrm{g} = \mathbf{e}_\mathrm{y}^\mathrm{b}\cdot\mathbf{e}_\mathrm{t} = (\mathbf{e}_z\times\mathbf{e}_\mathrm{x}^\mathrm{b})\cdot\mathbf{e}_\mathrm{t} = (\mathbf{e}_\mathrm{x}^\mathrm{b}\times\mathbf{e}_\mathrm{t})\cdot\mathbf{e}_z, \quad (22.21)$$

$$= \frac{1}{R_\mathrm{g}l_\mathrm{t}}\left(r_{\mathrm{B,x}}l_{\mathrm{t,y}} - r_{\mathrm{B,y}}l_{\mathrm{t,x}}\right). \quad (22.22)$$

This derivation involves the unit vectors $\mathbf{e}_\mathrm{x}^\mathrm{b}, \mathbf{e}_\mathrm{y}^\mathrm{b}$ and $\mathbf{e}_\mathrm{z}^\mathrm{b} = \mathbf{e}_z$ of the rotating reference frame $(x_\mathrm{b}, y_\mathrm{b}, z_\mathrm{b})$ and is illustrated in Fig. 22.10.

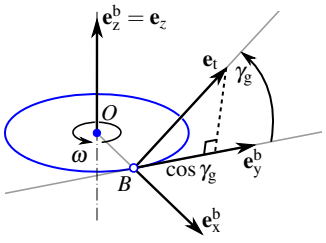

Fig. 22.10 Definition of the tether attachment angle γ_g for the ground rotor. The cosine of this angle is obtained as orthogonal projection of the tether unit vector $\mathbf{e}_\mathrm{t}$ onto the tangential unit vector $\mathbf{e}_\mathrm{y}^\mathrm{b}$

In a similar way, the tether attachment angle γ_k at the flying rotor can be computed from the unit vectors $\mathbf{e}_\mathrm{x}^\mathrm{a}, \mathbf{e}_\mathrm{y}^\mathrm{a}$ and $\mathbf{e}_\mathrm{z}^\mathrm{a} = \mathbf{e}_\mathrm{z}^\mathrm{k}$ of the rotating reference frame $(x_\mathrm{a}, y_\mathrm{a}, z_\mathrm{a})$ and the tether unit vector $\mathbf{e}_\mathrm{t}$ as

$$\cos\gamma_\mathrm{k} = \mathbf{e}_\mathrm{y}^\mathrm{a}\cdot\mathbf{e}_\mathrm{t} = (\mathbf{e}_\mathrm{z}^\mathrm{k}\times\mathbf{e}_\mathrm{x}^\mathrm{a})\cdot\mathbf{e}_\mathrm{t} = (\mathbf{e}_\mathrm{x}^\mathrm{a}\times\mathbf{e}_\mathrm{t})\cdot\mathbf{e}_\mathrm{z}^\mathrm{k}, \tag{22.23}$$

$$= \frac{1}{R_\mathrm{k} l_\mathrm{t}}\left[(r_{\mathrm{A,y}} l_{\mathrm{t,z}} - r_{\mathrm{A,z}} l_{\mathrm{t,y}})\sin\alpha + (r_{\mathrm{A,x}} l_{\mathrm{t,y}} - r_{\mathrm{A,y}} l_{\mathrm{t,x}})\cos\alpha\right]. \tag{22.24}$$

Physically, Eqs. (22.21) and (22.23) represent the contribution of the tether force to the dimensionless torque in the system. This kinematic expression will be used as a starting point for the analysis of the torque transfer in Sect. 22.6.

The derivations in this section are for a representative pair of tether attachment points. For the other pairs similar relations can be formulated by applying additional phase shifts to the phase angle ωt.

22.5.4 Parametric Case Study

The kinematics of the torque transmission system is fully described by the N distance vectors which connect the flying rotor to the ground rotor and which are given by Eq. (22.14) for a representative pair of tether attachment points. In the following the effect of the angular parameters $\alpha, \beta_\mathrm{s}, \beta, \delta$ and ωt on the geometry of a tether system with representative proportions $R_\mathrm{g}/R_\mathrm{k} = 1$ and $l_\mathrm{K}/R_\mathrm{k} = 2$ is analyzed.

The variation of the minimum and maximum tether lengths with the elevation angle is quantified in Fig. 22.11(left). At the limiting case of a vertical tether system, $\beta = 90°$, the axes of rotation of both rotors coincide and accordingly the tethers are of constant length $l_\mathrm{t,min} = l_\mathrm{t,max}$. For vanishing phase lag angle, $\delta = 0$, the tether

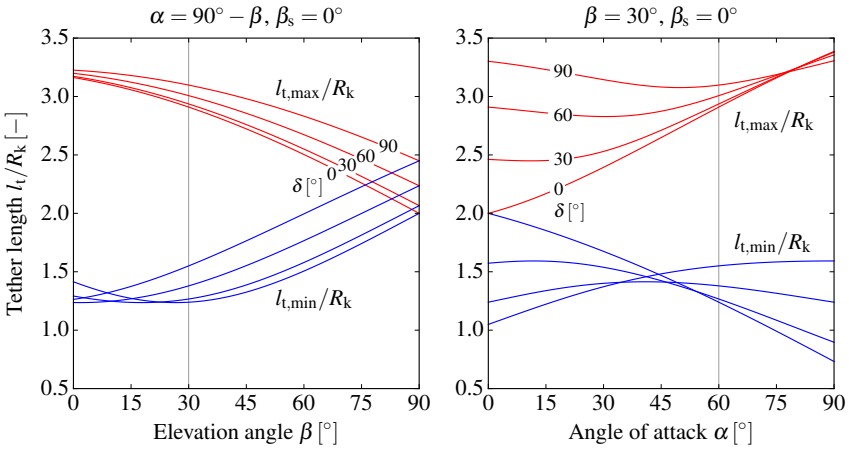

Fig. 22.11 Minimum and maximum tether lengths, $l_\mathrm{t,min}$ and $l_\mathrm{t,max}$, as functions of the elevation angle β (left) and angle of attack α (right) for $R_\mathrm{g}/R_\mathrm{k} = 1$ and $l_\mathrm{K}/R_\mathrm{k} = 2$. The left diagram illustrates the special case of kinematically coupled angle of elevation and angle of attack, e.g. by means of suspension lines, while the right diagram illustrates the study for a specific constant elevation angle. The vertical lines at 30° and respectively 60° indicate identical conditions in both diagrams

length equals the distance between the two rotors, $l_t = l_K$, and for increasing phase lag also the tether length increases continuously. For decreasing elevation angle the variation of tether length increases. At practically relevant values $30^\circ < \beta < 60^\circ$ the dimensionless length difference $\Delta l_t / R_k$ is roughly between 1.5 and 1.0.

The variation of the minimum and maximum tether lengths with the angle of attack of the flying rotor is quantified in Fig. 22.11(right) for a representative value of the elevation angle, $\beta = 30^\circ$, and a vanishing sideslip angle. At the limiting case of a horizontal flying rotor and vanishing phase lag the tethers are aligned with the axis of rotation and accordingly the tether length is constant. It should be noted that this holds only for the special case of $R_g/R_k = 1$ because for any other value the tethers are generally not aligned with the axis of rotation.

The variation of the tether attachment angles during one full revolution of the system is illustrated in Fig. 22.12. For the interpretation of the diagrams it is im-

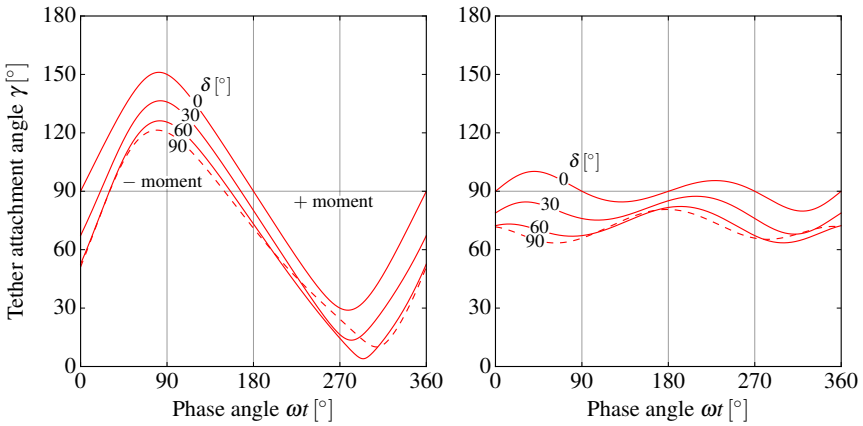

Fig. 22.12 Tether attachment angle γ at the ground rotor (left) and at the flying rotor (right) as functions of the phase angle ωt for $\beta = 30^\circ, \alpha = 60^\circ, \beta_s = 0, R_g/R_k = 1, l_K/R_k = 2$

portant to note that for $\gamma < 90^\circ$ the tensile force in the tether contributes a positive moment, acting in the direction of the rotation, while for $\gamma > 90^\circ$ it contributes a negative moment, acting against the direction of the rotation. At the limiting case $\gamma = 90^\circ$ the moment contribution vanishes (see also Fig. 22.10).

Figure 22.12(left) shows the tether attachment angle γ_g, as defined by Eq. (22.21), for different values of the phase lag angle. It can be seen that the step from $\delta = 0$ to 30° results in a consistent and nearly uniform shift of the sine-type curve to lower values. The steps from 30 to 60° and further to 90° follow this trend and increase the asymmetry of the curves with respect to the limiting case $\gamma = 90^\circ$, however, they are also characterized increasingly by nonlinear kinematic effects. The asymmetry with respect to $\gamma = 90^\circ$ directly affects the transfer of torque to the generator because it quantifies the net moment contribution of the corresponding force per revolution of

the system. It can be concluded that for the analyzed case a phase lag angle between 60 and 90° results in the best achievable moment contribution. The curve for $\delta = 0$ shows the expected change of sign of the moment contribution at $\omega t = 180$ and 360°, however, the extreme values $\gamma_{\max} = 151.1$ and $\gamma_{\min} = 28.9$ do not occur at $\omega t = 90$ and 270°, as one might expect, but at $\omega t = 81.6$ and 278.4°. This is a consequence of the geometric asymmetry of the revolving tether system tilted in downwind direction.

Figure 22.12(right) shows the tether attachment angle γ_k, as defined by Eq. (22.23), for different values of the phase lag angle. Compared to the ground rotor attachment angle the variation is substantially smaller, for this particular case almost one magnitude. Furthermore, the frequency of the variation is doubled, for example, the curve for $\delta = 0$ changes the sign of the moment contribution at $\omega = 90, 180, 270$ and 360°. For practically required values of the phase lag angle, as can be seen for $\delta \gtrsim 30°$, the moment contribution is shifted entirely to positive values.

This behavior can be explained by the fact that for the case of kinematically coupled angle of elevation and angle of attack, for which the axis of rotation of the flying rotor passes through the center of the ground rotor, the tether system attaches orthogonally to the flying rotor, which minimizes the kinematically induced variation of the attachment angle of the individual tethers and allows a stable counterbalancing of the aerodynamic moment. On the other hand the tether system attaches to the ground rotor at the elevation angle which causes a fundamental asymmetry of the moment transfer to the rotor and as consequence the tether attachment angle and the moment contribution of the tether force alternate periodically, as illustrated in Fig. 22.12. The torque transfer mechanism will be investigated in more detail in Sect. 22.6.

22.5.5 Conclusions

The objective of this section was to derive a kinematic model for the steady-state operation of the tensile torque transmission system. To achieve this, it was assumed that the system configuration in steady-state operation is known and can be described by the angle of attack α and sideslip angle β_s of the flying rotor, the elevation angle β of the kite center point, the phase lag angle δ of the ground rotor, the distances R_g and R_k of the tether attachment points from the centers of the ground and flying rotors, respectively, and the distance l_K of the kite center point from the origin. For such a prescribed operational state Eq. (22.14) describes the time evolution of the vector connecting the ground and flying rotor attachment points of the tether, Eq. (22.15) of the length of the tether, Eq. (22.17) of the reeling velocity of the tether and Eq. (22.21) of the attachment angle of the tether at the ground rotor.

The noncoaxial arrangement of the rotors and the phase lag distort the geometry of the tether system to an asymmetric state and introduce nonlinear kinematic effects. The parametric case study has shown how these effects intensify with increasing distortion of the tether system. Furthermore, the tether attachment angle

was identified as an important kinematic property for the moment transfer. Because the special case of kinematically coupled angle of elevation and angle of attack leads to nearly constant tether attachment geometry at the flying rotor, which is optimal for a stable torque transfer, we will only consider this configuration in the remainder of the chapter.

22.6 Power Transmission in Steady-State Operation

The aerodynamic force and moment of the ring kite are transferred to the ground conversion system by tensile forces only. The particular feature of the system is the power takeoff by two different, intrinsically coupled energy conversion mechanisms. The direct mechanism is based on the resultant moment that the tensile forces exert on the ground rotor, whereas the secondary mechanism is based on the length variation of the tethers. In this section a model for the power transmission characteristics of the tether system is formulated for steady-state operation. This model is used to assess the transmission efficiency as a function of the problem parameters, as well as the relation between transmitted torque and aerodynamic force. The focus of the analysis is on the tether system and not on the ring kite itself. It should be noted that the use of suspension lines is not considered in this analysis.

22.6.1 Energy Equation of the Single Tether

To assess the power transmission by the revolving tether system we first analyze the energy balance of the single tether. For this purpose the tether is cut free at the attachment points, as illustrated in Fig. 22.13. Neglecting the effects of aerodynamic

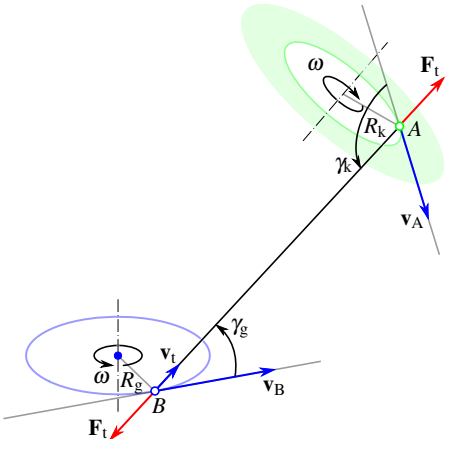

Fig. 22.13 Forces and velocities at the attachment points of a representative tether. The other tethers and their attachment points are not depicted. The attachment points A and B move with circumferential velocities $v_A = \omega R_k$ and $v_B = \omega R_g$. In the depicted situation the tether length is decreasing which requires the winch module at attachment point B to reel the tether in with a velocity v_t

drag and inertial forces and assuming that the tether is straight and inelastic, it can be concluded that the tensile forces at the two attachment points are of equal magnitude and pointing in opposite direction. In reference to Fig. 22.13 the energy equation can be formulated as

$$F_\mathrm{t} \cos\gamma_\mathrm{k}\, \omega R_\mathrm{k} = F_\mathrm{t} \cos\gamma_\mathrm{g}\, \omega R_\mathrm{g} + F_\mathrm{t} v_\mathrm{t}. \tag{22.25}$$

The left hand side represents the power transferred from the flying rotor to the tether by the circular motion of the attachment point A, while the first term on the right hand side represents the power transferred from the tether to the ground rotor by the circular motion of the attachment point B. The third contribution is the mechanical power that is transferred to the winch module that is attached to the rotor at point B. If we define a characteristic power of the tensile torque transmission problem as $F_\mathrm{t}\omega R_\mathrm{k}$ and divide Eq. (22.25) by this expression we obtain the dimensionless equation

$$\cos\gamma_\mathrm{k} = \cos\gamma_\mathrm{g} \frac{R_\mathrm{g}}{R_\mathrm{k}} + \frac{v_\mathrm{t}}{\omega R_\mathrm{k}}. \tag{22.26}$$

This fundamental equation relates the two tether attachment angles and the dimensionless tether reeling velocity introduced in the context of Eq. (22.18).

The variation of the three dimensionless power contributions is shown in Fig. 22.14. The case of vanishing phase lag is depicted in Fig. 22.14(left) and, as expected, in-

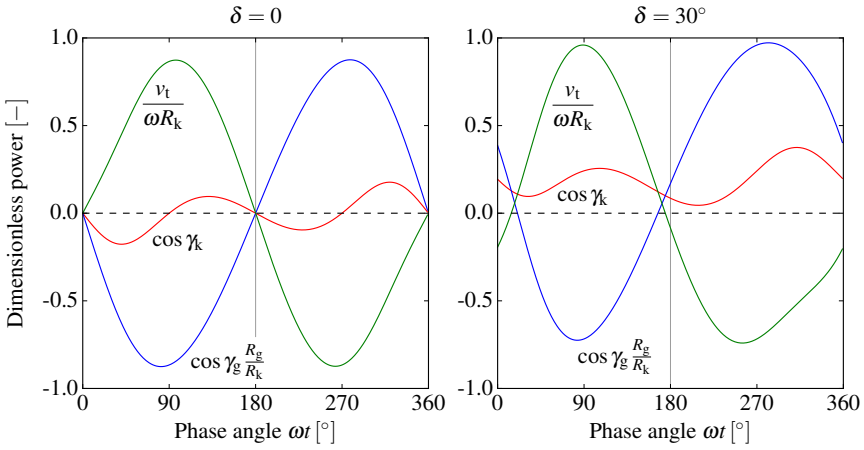

Fig. 22.14 Kinematic modulation of the dimensionless power balance at the tether during one revolution for $R_\mathrm{g}/R_\mathrm{k} = 1, l_\mathrm{K}/R_\mathrm{k} = 2, \beta = 30°, \beta_\mathrm{s} = 0°$ and $\alpha = 60°$. The dashed line represents the sum of all contributions

dicates that the net power that is transferred from the flying rotor to the tether during one revolution is close to zero. As consequence, the other two power contributions, the shaft power contribution to the ground rotor and the reeling power transferred to the winch module have to cancel out each other. When applying a phase lag angle of $\delta = 30°$ the net power transferred from the flying rotor to the tether is positive,

which is indicated by the upwards shift of the corresponding curve. It is obvious from Fig. 22.14 that for this particular case, the input power is balanced by comparatively large variations of the output power contributions. In the real system, the associated losses would be significant, which is a point of concern.

It is important to note that Eq. (22.25) does not provide any information about the actual values of the tensile force and their power contributions but only the relative distribution of these contributions depending on the instantaneous kinematics of the system. To derive the actual values of the tensile forces the equations of motion of the ground and flying rotors have to be considered, which is the topic of the following section.

22.6.2 Quasi-Steady Motion of the Flying Rotor

Because of the relatively low mass of the flying rotor and the tethers the airborne system adjusts rapidly to force imbalances. The resulting quasi-steady motion is governed by the equilibrium of the aerodynamic force distribution, the tether forces and gravitational forces. If we neglect, for simplicity, the effect of gravity, the equilibrium of forces and moments acting on the flying rotor can be formulated as

$$\mathbf{F}_\mathrm{a} = -\sum_{i=1}^{N} \mathbf{F}_{\mathrm{t,i}}, \tag{22.27}$$

$$\mathbf{M}_\mathrm{a} = -\sum_{i=1}^{N} (\mathbf{r}_{\mathrm{A,i}} - \mathbf{r}_\mathrm{K}) \times \mathbf{F}_{\mathrm{t,i}}, \tag{22.28}$$

which is illustrated in Fig. 22.15.

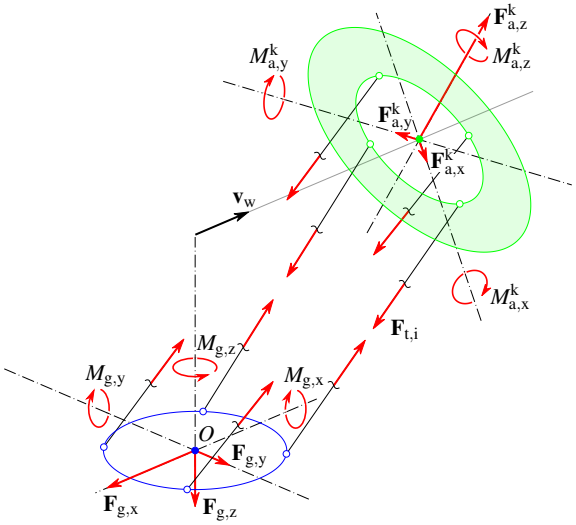

Fig. 22.15 Forces and moments acting on the ground and flying rotors. The resultant aerodynamic force and moment are represented by their components in the kite reference frame. The reaction force and moment acting in the bearing mechanism of the ground rotor are represented by their components in the wind reference frame. $M_{\mathrm{g,z}}$ denotes the transmitted moment that is available for conversion into electricity

The resultant aerodynamic force and moment vectors, $\mathbf{F}_\mathrm{a}$ and $\mathbf{M}_\mathrm{a}$, are represented by their components in the kite reference frame. $\mathbf{F}^\mathrm{k}_\mathrm{a,z}$ is the main force component acting along the rotor axis, while $\mathbf{F}^\mathrm{k}_\mathrm{a,x}$ and $\mathbf{F}^\mathrm{k}_\mathrm{a,y}$ are the two transverse components. Accordingly, $M^\mathrm{k}_\mathrm{a,z}$ is the main moment component acting around the rotor axis, while $M^\mathrm{k}_\mathrm{a,y}$ and $M^\mathrm{k}_\mathrm{a,x}$ are the components around the pitch and roll axes of the kite. The z_k-components of the aerodynamic force and moment are the two key functional elements of the RRP system, responsible for tensioning the tether system and for generating torque that is transferred to the ground to be converted into electricity.

The aerodynamic loading of the flying rotor is balanced by the N tether forces $\mathbf{F}_\mathrm{t,i}$. The calculation of the individual moment contributions specified by Eq. (22.28) differs from the calculation of the tether attachment angle γ_k, as specified by Eq. (22.23), only by the additional multiplicative factors $F_\mathrm{t,i}$, the magnitudes of the tether forces.

The difficulty in solving the quasi-steady equilibrium equations for the unknown tether forces $\mathbf{F}_\mathrm{t,i}$ comes from the fact that except for the design parameters $R_\mathrm{g}, R_\mathrm{k}$ and $R_\mathrm{k,o}$, the actuated tether lengths $l_\mathrm{t,i}$ and the wind velocity v_w all other problem parameters, $\alpha, \beta_\mathrm{s}, \beta, \phi, \delta, \omega$ and l_K have to be regarded as degrees of freedom, subject to additional kinematic coupling conditions. This differs from the starting point of the kinematic analysis in Sect. 22.5 where we assumed steady-state operation of the system with known values of these problem parameters.

22.6.3 Approximate Solution of Steady-State Operation

Instead of attempting to solve the problem of quasi-steady motion of the flying rotor exactly, as described by Eqs. (22.27) and (22.28), we derive an approximate solution of the idealized problem of steady-state operation. Following the approach described in Sect. 22.5 we consider only the principal force axis of the system, which is the axis of rotation of the flying rotor. To fulfill the force equilibrium in this axis we assume that the components of the tether forces in this direction are all of equal magnitude, which is formally expressed by the conditions

$$\mathbf{F}_\mathrm{t,i} \cdot \mathbf{e}^\mathrm{k}_\mathrm{z} = -\frac{F^\mathrm{k}_\mathrm{a,z}}{N}, \qquad i = 1, \ldots, N. \tag{22.29}$$

Representing the force vectors as $\mathbf{F}_\mathrm{t,i} = F_\mathrm{t,i}\mathbf{e}_\mathrm{t,i}$, where $\mathbf{e}_\mathrm{t,i}$ represents the unit vector along tether i, the individual force magnitudes can be derived as

$$F_\mathrm{t,i} = -\frac{F^\mathrm{k}_\mathrm{a,z}}{N\mathbf{e}_\mathrm{t,i} \cdot \mathbf{e}^\mathrm{k}_\mathrm{z}}, \qquad i = 1, \ldots, N. \tag{22.30}$$

The tether forces defined by these equations exactly balance the axial aerodynamic force component $F^\mathrm{k}_\mathrm{a,z}$. Furthermore, the resultant roll and pitch moments of the tether forces vanish because the geometric center of the tether attachment points coincides

with the kite center K and the moment-contributing force components $\mathbf{F}_{\mathrm{t,i}} \cdot \mathbf{e}_{\mathrm{z}}^{\mathrm{k}}$ are all equal. As consequence, the corresponding aerodynamic moment components $M_{\mathrm{a,x}}^{\mathrm{k}}$ and $M_{\mathrm{a,y}}^{\mathrm{k}}$ vanish and

$$M_{\mathrm{a}} = M_{\mathrm{a,z}}^{\mathrm{k}}. \tag{22.31}$$

However, the tether forces defined by Eq. (22.30) induce transverse force components which need to be balanced by the transverse aerodynamic force components $\mathbf{F}_{\mathrm{a,x}}^{\mathrm{k}}$ and $\mathbf{F}_{\mathrm{a,y}}^{\mathrm{k}}$ and which lead to transverse compensating motions. We can derive the following expressions for the ratios of the transverse aerodynamic force components to the axial force component

$$\frac{F_{\mathrm{a,x}}^{\mathrm{k}}}{F_{\mathrm{a,z}}^{\mathrm{k}}} = \frac{1}{N}\sum_{i=1}^{N} \frac{\mathbf{e}_{\mathrm{t,i}} \cdot \mathbf{e}_{\mathrm{x}}^{\mathrm{k}}}{\mathbf{e}_{\mathrm{t,i}} \cdot \mathbf{e}_{\mathrm{z}}^{\mathrm{k}}}, \tag{22.32}$$

$$\frac{F_{\mathrm{a,y}}^{\mathrm{k}}}{F_{\mathrm{a,z}}^{\mathrm{k}}} = \frac{1}{N}\sum_{i=1}^{N} \frac{\mathbf{e}_{\mathrm{t,i}} \cdot \mathbf{e}_{\mathrm{y}}^{\mathrm{k}}}{\mathbf{e}_{\mathrm{t,i}} \cdot \mathbf{e}_{\mathrm{z}}^{\mathrm{k}}}. \tag{22.33}$$

The moment components acting around the rotational axes of the flying rotor and the ground rotor can be evaluated as

$$\frac{M_{\mathrm{a}}}{R_{\mathrm{k}} F_{\mathrm{a,z}}^{\mathrm{k}}} = \frac{1}{N}\sum_{i=1}^{N} \frac{(\mathbf{e}_{\mathrm{x,i}}^{\mathrm{a}} \times \mathbf{e}_{\mathrm{t,i}}) \cdot \mathbf{e}_{\mathrm{z}}^{\mathrm{k}}}{\mathbf{e}_{\mathrm{t,i}} \cdot \mathbf{e}_{\mathrm{z}}^{\mathrm{k}}} = \frac{1}{N}\sum_{i=1}^{N} \frac{\cos\gamma_{\mathrm{k,i}}}{\mathbf{e}_{\mathrm{t,i}} \cdot \mathbf{e}_{\mathrm{z}}^{\mathrm{k}}}, \tag{22.34}$$

$$\frac{M_{\mathrm{g,z}}}{R_{\mathrm{k}} F_{\mathrm{a,z}}^{\mathrm{k}}} = \frac{1}{N}\frac{R_{\mathrm{g}}}{R_{\mathrm{k}}}\sum_{i=1}^{N} \frac{(\mathbf{e}_{\mathrm{x,i}}^{\mathrm{b}} \times \mathbf{e}_{\mathrm{t,i}}) \cdot \mathbf{e}_{z}}{\mathbf{e}_{\mathrm{t,i}} \cdot \mathbf{e}_{\mathrm{z}}^{\mathrm{k}}} = \frac{1}{N}\frac{R_{\mathrm{g}}}{R_{\mathrm{k}}}\sum_{i=1}^{N} \frac{\cos\gamma_{\mathrm{g,i}}}{\mathbf{e}_{\mathrm{t,i}} \cdot \mathbf{e}_{\mathrm{z}}^{\mathrm{k}}}, \tag{22.35}$$

using the product $R_{\mathrm{k}} F_{\mathrm{a,z}}^{\mathrm{k}}$ as a characteristic moment of the tensile torque transmission problem, for normalization of the moment components.

To compute an approximate solution of the steady-state operation of the flying rotor we regard the transverse aerodynamic force components given by Eqs. (22.32) and (22.33) as perturbations. Based on the formulation of an optimization problem we minimize the perturbations to find the best solution. Starting point of the optimization is a specific configuration defined by the dimensionless parameters β, δ and $l_{\mathrm{K}}/R_{\mathrm{k}}$. The orientation of the flying rotor with respect to the wind, defined by the flow angles α and β_{s}, is varied to minimize the perturbations. Because the transverse forces oscillate periodically we use the following objective function

$$\begin{aligned} f(\alpha,\beta_{\mathrm{s}}) = {} & \left|\max F_{\mathrm{a,x}}^{\mathrm{k}} - \min F_{\mathrm{a,x}}^{\mathrm{k}}\right| + \left|\max F_{\mathrm{a,x}}^{\mathrm{k}} + \min F_{\mathrm{a,x}}^{\mathrm{k}}\right| \\ & + \left|\max F_{\mathrm{a,y}}^{\mathrm{k}} - \min F_{\mathrm{a,y}}^{\mathrm{k}}\right| + \left|\max F_{\mathrm{a,y}}^{\mathrm{k}} + \min F_{\mathrm{a,y}}^{\mathrm{k}}\right| \end{aligned} \tag{22.36}$$

applying the min and max operators to to the complete interval $0^\circ \leq \omega t \leq 360^\circ$. The solution of the optimization problem is the combination of flow angles α and β_{s} that minimizes Eq. (22.36). The solution is approximative because the residual transverse forces are causing compensating motions which are not taken into ac-

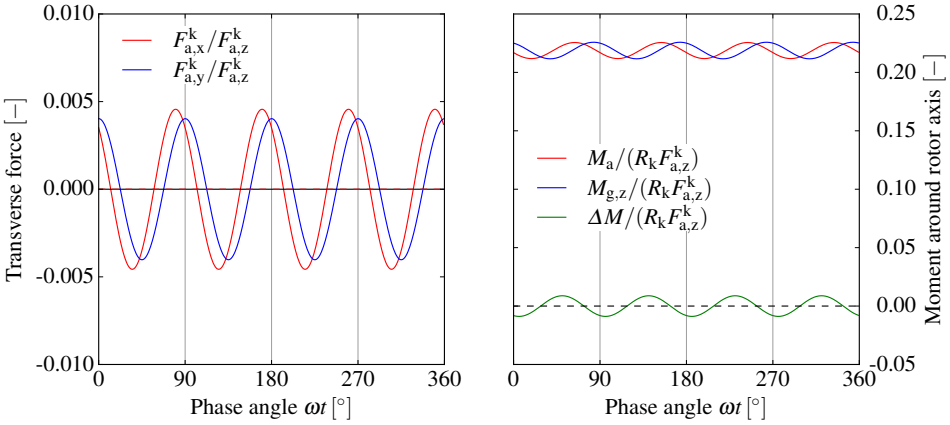

Fig. 22.16 Steady-state operation of the flying rotor with dimensionless transverse force components (left) and moment components around the rotor axes (right) for $N = 4$, $R_g/R_k = 1$, $l_K/R_k = 2$, $\beta = 30^\circ$ and $\delta = 30^\circ$. Initial values for the minimum search are $\alpha_0 = 60^\circ$, $\beta_{s,0} = 0^\circ$ and the solution values are $\alpha = 62.36^\circ$, $\beta_s = 4.38^\circ$

count in the analysis. However, the following results indicate that the effect of the compensating motions is minor and can be neglected.

A representative result is illustrated in Fig. 22.16. The left diagram shows the periodic variations of the transverse force components acting on the flying rotor which are of the order of 1% of the axial force component. The mean values $\overline{F}^k_{a,x}$ and $\overline{F}^k_{a,y}$ vanish. The right diagram shows the periodic variations of the generated aerodynamic moment and the usable moment at the ground rotor, as well as the difference of both curves. It should be noted that the product $R_k F_a$ is only a reference moment used for normalization and does not have any other physical meaning than providing a characteristic order of magnitude value. Compared to the single-tether behavior, as shown in Figs. 22.12 and 22.14, the frequency of the oscillation is increased by a factor of $N = 4$, which is caused by the superposition of phase-shifted data.

It can be recognized that the periodic variations of the moments $M^k_{a,z}$ and $M_{g,z}$ are shifted in phase by the angle $\delta = 30^\circ$. The moment difference $\Delta M = M_a - M_{g,z}$ is associated with the periodic variation of the net mechanical energy processed by the winch modules. For a single tether this relationship is given by Eq. (22.26). For the entire system the normalized moment difference is computed as

$$\frac{\Delta M}{R_k F^k_{a,z}} = \frac{1}{N \omega R_k} \sum_{i=1}^{N} \frac{v_{t,i}}{\mathbf{e}_{t,i} \cdot \mathbf{e}^k_z}. \tag{22.37}$$

It can further be recognized that the mean value of the moment difference for a full revolution of the tether system is zero, which means that the average moments are identical,

$$\overline{M}_{\mathrm{a}} = \overline{M}_{\mathrm{g,z}}. \tag{22.38}$$

This essentially means that the transmission efficiency for the ideal system in steady-state operation is, as expected, 100%. For a real system the electrical interconnection of the winch modules will cause conversion losses that will significantly reduce the transmission efficiency. Based on the presented analytic modeling framework these losses as well as all other types of losses (tether aerodynamic drag, bearing friction losses, etc.) can be taken into account in a future study. It is also obvious from the analysis that the number of peripheral tethers affects the frequency of variation the instantaneous kinematic properties and the associated forces and moments but has no effect on the mean values.

In Fig. 22.17 the representative example is expanded to the full range of values of the phase lag angle δ. The left diagram shows the computed values of the flow

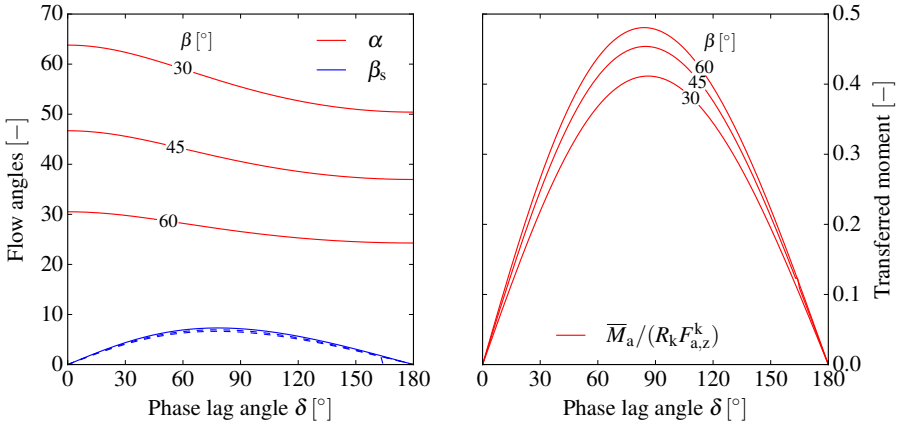

Fig. 22.17 Flow angles α and β_{s} (left) and dimensionless average moment $\overline{M}_{\mathrm{a}}/(R_{\mathrm{k}}F^{\mathrm{k}}_{\mathrm{a,z}})$ (right) as functions of the phase lag angle δ, for various values of the elevation angle β and for $N = 4$, $R_{\mathrm{g}}/R_{\mathrm{k}} = 1$ and $l_{\mathrm{K}}/R_{\mathrm{k}} = 2$. Initial values for the minimum search are $\alpha_0 = 90° - \beta$ and $\beta_{\mathrm{s},0} = 0°$

angles α and β_{s}, while the right diagram shows the average moment $\overline{M}_{\mathrm{a}}$ normalized by the reference value $R_{\mathrm{k}}F^{\mathrm{k}}_{\mathrm{a,z}}$. It can be recognized that for the limiting values $\delta = 0°$ and $\delta = 180°$ no moment can be transmitted, while the maximum moment $\overline{M}_{\mathrm{a,max}}$ can be transmitted for δ_{max}. For this particular example we have $\delta_{\mathrm{max}} \lesssim 90°$. This maximum moment increases with increasing elevation angle β.

22.6.4 Requirements for the rotor aerodynamic design

To this point the focus of the analysis has been the transmission of torque from the flying rotor to the ground rotor. From Fig. 22.17(right), or similar diagrams for

other combinations of problem parameters, the possible range of the transmittable aerodynamic moment $\overline{M}_{\mathrm{a}}$ can be determined as a function of the aerodynamic force $F^{\mathrm{k}}_{\mathrm{a,z}}$. It can further be determined how within this range the moment varies with the phase lag angle δ. From Fig. 22.17(left) we can determine the required orientation of the flying rotor to transmit this moment to the ground while in a steady state of operation. However, these parameters also have a major effect on the aerodynamics of the flying rotor. In fact, the two key functional components of the RRP system, the generation of the aerodynamic moment and the transmission of this moment to the ground rotor, need to be matched properly to achieve steady-state operation. It is the purpose of this section to derive the top-level requirements for the rotor aerodynamic design. The specific implementation of the rotary ring kite is however not within the scope of the present analysis.

To determine the aerodynamic characteristics of the ring kite it is useful to decompose the resultant aerodynamic force $\mathbf{F}_{\mathrm{a}}$ into lift and drag components. By definition the drag force $\mathbf{D}$ is aligned with the apparent wind velocity $\mathbf{v}_{\mathrm{a}} = \mathbf{v}_{\mathrm{w}} - \mathbf{v}_{\mathrm{k}}$, while the lift force $\mathbf{L}$ is perpendicular to the drag component. Assuming that the velocity of the kite $\mathbf{v}_{\mathrm{k}} = d\mathbf{r}_{\mathrm{K}}/dt$ can be neglected during steady-state operation we can use the components of $\mathbf{F}_{\mathrm{a}}$ in the wind reference frame to calculate

$$L = \sqrt{F^2_{\mathrm{a,y}} + F^2_{\mathrm{a,z}}}, \tag{22.39}$$

$$D = F_{\mathrm{a,x}}. \tag{22.40}$$

Using the transformation matrix $\mathbf{T}_{\mathrm{wk}}$ defined by Eq. (22.11) the components of the instantaneous aerodynamic force and its mean value can be calculated as

$$\mathbf{F}_{\mathrm{a}} = \begin{bmatrix} F_{\mathrm{a,x}} \\ F_{\mathrm{a,y}} \\ F_{\mathrm{a,z}} \end{bmatrix} = \mathbf{T}_{\mathrm{wk}} \begin{bmatrix} F^{\mathrm{k}}_{\mathrm{a,x}} \\ F^{\mathrm{k}}_{\mathrm{a,y}} \\ F^{\mathrm{k}}_{\mathrm{a,z}} \end{bmatrix} \quad \text{and} \quad \overline{\mathbf{F}}_{\mathrm{a}} = \begin{bmatrix} \cos\beta_{\mathrm{s}} \sin\alpha \\ \sin\beta_{\mathrm{s}} \sin\alpha \\ \cos\alpha \end{bmatrix} F^{\mathrm{k}}_{\mathrm{a,z}}, \tag{22.41}$$

because $\overline{F}^{\mathrm{k}}_{\mathrm{a,x}} = \overline{F}^{\mathrm{k}}_{\mathrm{a,y}} = 0$. Furthermore, the mean values of lift and drag can be calculated as functions of the axial aerodynamic force component and the flow angles

$$L = F^{\mathrm{k}}_{\mathrm{a,z}} \sqrt{\sin^2\beta_{\mathrm{s}} \sin^2\alpha + \cos^2\alpha}, \tag{22.42}$$

$$D = F^{\mathrm{k}}_{\mathrm{a,z}} \cos\beta_{\mathrm{s}} \sin\alpha, \tag{22.43}$$

which are related by

$$\frac{L}{D} = \frac{\sqrt{\sin^2\beta_{\mathrm{s}} \sin^2\alpha + \cos^2\alpha}}{\cos\beta_{\mathrm{s}} \sin\alpha}. \tag{22.44}$$

Equations (22.42), (22.43) and (22.44) define the required aerodynamic characteristics of the airborne system as functions of the axial aerodynamic force $F^{\mathrm{k}}_{\mathrm{a,z}}$, the angle of attack α and the sideslip angle β_{s}.

The dimensional forces and the moment are generally expressed in terms of dimensionless aerodynamic coefficients

$$L = \frac{1}{2}\rho C_{\mathrm{L}} v_{\mathrm{w}}^2 S, \qquad \text{with} \quad C_{\mathrm{L}} = C_{\mathrm{L}}(\alpha_{\mathrm{eff}}, \lambda), \tag{22.45}$$

$$D = \frac{1}{2}\rho C_{\mathrm{D}} v_{\mathrm{w}}^2 S \qquad \text{with} \quad C_{\mathrm{D}} = C_{\mathrm{D}}(\alpha_{\mathrm{eff}}, \lambda), \tag{22.46}$$

$$M_{\mathrm{a}} = \frac{1}{2}\rho C_{\mathrm{M}} v_{\mathrm{w}}^2 R_{\mathrm{k,o}} S \qquad \text{with} \quad C_{\mathrm{M}} = C_{\mathrm{M}}(\alpha_{\mathrm{eff}}, \lambda), \tag{22.47}$$

where $S = \pi(R_{\mathrm{k,o}}^2 - R_{\mathrm{k}}^2)$ is the swept rotor area, λ is the tip speed ratio defined by

$$\lambda = \frac{\omega R_{\mathrm{k,o}}}{v_{\mathrm{w}}} \tag{22.48}$$

and α_{eff} is the angle between wind velocity vector $\mathbf{v}_{\mathrm{w}}$ and the rotor disk, defined by

$$\cos\alpha_{\mathrm{eff}} = \mathbf{e}_{\mathrm{x}}^{\mathrm{k}} \cdot \mathbf{e}_x, \tag{22.49}$$

$$\alpha_{\mathrm{eff}} = \arccos(\cos\beta_{\mathrm{s}} \cos\alpha). \tag{22.50}$$

The sideslip angle and the angle of attack contribute equally to α_{eff} because of the ring-shaped swept area of the rotor. For a static wing this is not the case and the effects of sideslip angle and angle of attack have to be differentiated. It can be shown that the axial moment coefficient C_{M} is formally related to the more customary power coefficient C_{p} [13, p. 45] by the relation

$$C_{\mathrm{M}} = \frac{C_{\mathrm{p}}}{\lambda}. \tag{22.51}$$

It should also be noted that the induced velocity is not taken into account in the above simplified aerodynamic analysis. An excellent follow-up study in this direction is [13, p. 99–103] which assesses Glauert's momentum theory for a gyrocopter in autorotation.

Aside of the influence of the operational parameters α_{eff} and λ, the aerodynamic coefficients depend also on design parameters, for example, the solidity σ of the rotor. Because the rotor aerodynamic design is out of the scope of the present study the analysis will not be continued at this point. It should be noted though that rotary kites with flexible wings have not been studied scientifically so far.

It has to be assumed that the aerodynamic characteristics required for steady-state operation of the tensile torque transmission system, namely Eqs. (22.42), (22.43) and (22.44), can not necessarily be achieved by a specific design of the ring kite. This problem can be overcome by first designing the ring kite for the required aerodynamic moment and then, in a second step, designing an additional lifting kite which is tethered to the center of the ring kite and which supplements the aerodynamic characteristics of the ring kite to meet the overall requirements for the combined system.

22.6.5 Conceptual Design Example

In this section we outline a conceptual design process based on the developed modeling framework. Starting point is a tensile torque transmission system with a given geometry. We chose the intermediate-scale system defined in Table 22.4. The value

Table 22.4 Geometric and operational parameters of an intermediate-scale tensile torque transmission system. This configuration is also portrayed in Fig. 22.9

Parameter name	Symbol	Value	Unit
Ground rotor diameter	d_g	50	m
Flying rotor inner diameter	d_k	40	m
Distance between rotors	l_K	100	m
Elevation angle	β	30	deg
Phase lag ground rotor	δ	45	deg
Wind speed	v_w	12	m/s
Angular speed	ω	2.05	rad/s
Nominal power	P	1.4	MW

of the phase lag angle is set well below the limiting value for maximum torque transfer, δ_max to ensure good control behavior. From Table 22.4 we get

$$\frac{R_\mathrm{g}}{R_\mathrm{k}} = 1.25 \tag{22.52}$$

$$\frac{l_\mathrm{K}}{R_\mathrm{k}} = 5. \tag{22.53}$$

In a first step we calculate the aerodynamic moment that is required for transmitting the nominal power P at an angular speed ω of the rotor as

$$M_\mathrm{a} = \frac{P}{\omega} = 683\,\mathrm{kNm}. \tag{22.54}$$

We then determine the orientation of the flying rotor, in terms of the flow angles α and β_s, which minimizes the transverse perturbation forces defined by Eqs. (22.32) and (22.33). To compute this best approximation of steady-state operation we minimize the objective function defined by Eq. (22.36). Starting from the initial values $\alpha_0 = 60^\circ$ and $\beta_{\mathrm{s},0} = 0^\circ$ the iterative optimization procedure leads to the values

$$\alpha = 60.08^\circ, \tag{22.55}$$

$$\beta_\mathrm{s} = 1.05^\circ, \tag{22.56}$$

which reduce the oscillation amplitudes of $F^\mathrm{k}_\mathrm{a,x}/F^\mathrm{k}_\mathrm{a,z}$ and $F^\mathrm{k}_\mathrm{a,y}/F^\mathrm{k}_\mathrm{a,z}$ to below 0.05%. From Eq. (22.34) we can then calculate

$$\frac{M_\mathrm{a}}{R_\mathrm{k} F^\mathrm{k}_\mathrm{a,z}} = 0.1365, \tag{22.57}$$

which, using Eq. (22.54) and the value of R_k can be solved for the axial aerodynamic force

$$F_{\mathrm{a,z}}^{\mathrm{k}} = 250\,\mathrm{kN}. \tag{22.58}$$

Using Eqs. (22.42), (22.43) and (22.44) we can now compute the lift and drag force as

$$L = 125\,\mathrm{kN}, \tag{22.59}$$
$$D = 217\,\mathrm{kN}, \tag{22.60}$$
$$L/D = 0.576 \tag{22.61}$$

It is important to note that the numerical values given by Eqs. (22.58), (22.59) and (22.60) are not the result of an aerodynamic analysis but instead are required to transmit the aerodynamic moment specified by Eq. (22.54) to the ground rotor while maintaining a steady state of operation of the revolving tether system.

As a next step we analyze the aerodynamic requirements of the airborne subsystem. For conventional wind turbines the tip speed is generally limited by a noise constraint. In [13, p. 339] this tip speed limit is given as 65 m/s. Considering the value of ω listed in Table 22.4 and using a tip speed limit of ≈ 70 m/s we can calculate the outer diameter of the rotor, the swept area of the rotor and from Eq. (22.48) the tip speed ratio as

$$d_{\mathrm{k,o}} = 70\,\mathrm{m}, \tag{22.62}$$
$$S = 2592\,\mathrm{m}^2, \tag{22.63}$$
$$\lambda = 5.98. \tag{22.64}$$

Based on these values we can compute the aerodynamic coefficients from Eqs. (22.45), (22.46), (22.47) and (22.51) as

$$C_\mathrm{L} = 0.546, \tag{22.65}$$
$$C_\mathrm{D} = 0.948, \tag{22.66}$$
$$C_\mathrm{M} = 0.0854, \tag{22.67}$$
$$C_\mathrm{p} = 0.51. \tag{22.68}$$

The practical design of a ring kite would aim to achieve the required moment coefficient specified by Eq. (22.67) and then, in a second step, supplement its lift and drag forces by tethering an additional lifting kite to the center of the ring kite, as explained in Sect. 22.6.4.

22.6.6 Design Recommendations and Conclusions

The geometric proportions of the tensile torque transmission system have a decisive role. It is evident that the longer the tether system and the smaller the ground ro-

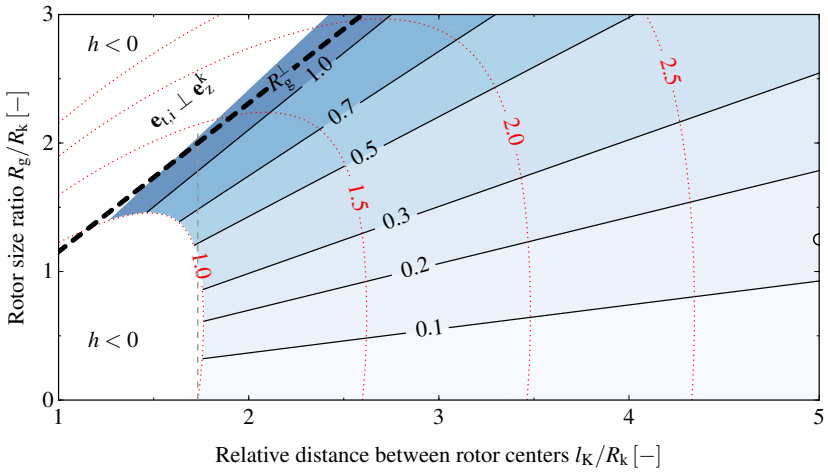

Fig. 22.18 Transferable aerodynamic moment $M_a/(R_k F_{a,z}^k)$ as function of the relative distance l_K/R_k between rotor centers and the rotor size ratio R_g/R_k for $\beta = 30°$, $\delta = 45°$. The colored contour plot and the solid black isolines cover only valid regions with positive ground distance of the tether attachments on the flying rotor ($h > 0$). The dashed line $R_g^\perp$ marks the condition of maximum transferable moment which is also a validity limit for the approximate solution of steady-state operation. The dotted red isolines mark the condition of ground contact for different values of the relative outer size $R_{k,o}/R_k$ of the flying rotor. The limiting isoline $(R_{k,o}/R_k)_{h=0} = 1$ coincides with the border of the contour plot. The dashed line at $l_K/R_k = \cot\beta \approx 1.73$ is the reference for the lower limit, for $\alpha = 90° - \beta$

tor the lower the transferable torque. The fundamental relationship is quantified by Eq. (22.26) which describes the influence of the tether attachment angles and the rotor size ratio. To support this recommendation quantitatively we have computed the transferable aerodynamic moment as a function of the geometric proportions of the tether system. The result of this analysis is illustrated in Fig. 22.18 for a system with representative elevation angle and phase lag angle. The contour plot and the solid isolines show that the transferable moment decreases for increasing distance between the rotors and that it increases with increasing size of the ground rotor. The diagram also includes the condition of ground contact of the flying rotor for different values of its relative outer size $R_{k,o}/R_k$. As shown in Fig. 22.19 this condition $(R_{k,o}/R_k)_{h=0}$ can be derived from the ground distance function

$$\frac{h}{R_k} = \frac{l_K}{R_k}\sin\beta - \frac{R_{k,o}}{R_k}\sin\alpha, \tag{22.69}$$

by setting $h = 0$ and solving for $R_{k,o}/R_k$. For example, if we consider a system with a relative outer size $R_{k,o}/R_k = 2$ only the region to the right of the dotted isoline labeled by the value $(R_{k,o}/R_k)_{h=0} = 2$ is physically feasible because of positive ground distance ($h > 0$). The data point at $l_K/R_k = 5$ and $R_g/R_k = 1.25$ refers to the specific calculation example in Sect. 22.6.5 which results in values $M_a/(R_k F_{a,z}^k) =$

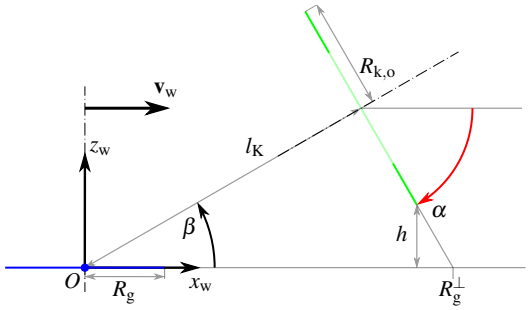

Fig. 22.19 Calculation of the distance h of the flying rotor from the ground. The specific illustrated geometric case has been described in Sect. 22.6.5. Because of the relatively large value of l_K/R_k the sideslip angle is in this case small ($\beta_s < 1°$) and the axis of the flying rotor approximately points to the origin ($\alpha = 90° - \beta$)

0.1365 and $(R_{k,o}/R_k)_{h=0} = 2.88$. A general conclusion from Fig. 22.18 is that an increasing size of the flying rotor requires generally an increasing distance between the rotors.

The deviation of the limiting isoline $(R_{k,o}/R_k)_{h=0} = 1$ from the dashed reference line at $l_K/R_k = \cot\beta \approx 1.73$ indicates how much the angle of attack α in steady-state operation deviates from the value $\alpha = 90° - \beta = 60°$. For $1.2 < R_g/R_k < 1.8$ the physically feasible region extends to values far below $l_K/R_k = 1.73$. This indicates that for these geometric proportions the flying rotor has an increased ground clearance as consequence of a relatively low angle of attack.

The dashed line in Fig. 22.18 marks the condition where for $\alpha = 90° - \beta$ the flying rotor plane touches the ground rotor. Considering Fig. 22.19 where this point is marked as $R_g^\perp$ the equation of the limiting line can be derived as

$$\frac{R_g^\perp}{R_k} = \frac{1}{\cos\beta}\frac{l_K}{R_k} = 1.155\frac{l_K}{R_k}. \tag{22.70}$$

Above this line the geometric proportions of the system are such that the revolving tethers pass through constellations in which they are momentarily orthogonal to the axis of the flying rotor. In this specific situation the fundamental assumption on which the approximate solution of steady-state operation is based, Eq. (22.30), becomes singular which introduces large artificial forces in the system. However, this anomaly of the theoretical model occurs in a region of the design space that has to be avoided for the sake of operational stability and for this reason the region is excluded as an invalid region ($\mathbf{e}_{t,i} \perp \mathbf{e}_z^k$).

It is obvious from Fig. 22.18 that the size of the flying rotor cannot be much larger than the diameter of the ground rotor if a practically significant torque is to be transferred. This has been confirmed also by the experimental tests. From a rotor aerodynamics point of view, the rotational speed ω = 2.05 rad/s, implies a tip speed ratio of around 6, which is a typical value for conventional wind turbines, and which is achievable with rigid wings. Lower values of the tip speed ratio, for example 4, are achievable with soft wings.

The Parotor should be restudied in all possible variants, including soft and rigid rotors, parachutes with a large opening [24] (with a diameter of 2 to 3 times the wing

span), including also some adaptations of centrifugally stiffened rotors [18, 22, 29], and above all C-shaped modular rigid structures with hinges [19] rotor components. Wings or blades should sweep more area and travel faster, like kites making loops [4], but within the rotating structure.

22.7 Current and Future Investigations

The focus of the present study has been the technical feasibility of the proposed RRP system. We have used a small-scale test setup to demonstrate the fundamental working principles and a theoretical model of the revolving tether system to show that steady-state operation is in principle feasible for a specific combination of design and operational parameters. A next important development step will be the design of a rotary ring kite and lifting kite combination with specific aerodynamic characteristics. Of similar importance will be the design of a rotating reel system with efficient energetic balancing of the interconnected winch modules. A possible realization could be mechanical coupling of the winch modules using differential reeling to avoid the additional losses of electrical conversion. With the worked out conceptual and preliminary designs of these two key technology components the assessment of the energy harvesting potential of the RRP system can be further refined.

Next to the overall system design and the conversion performance we will also investigate other important aspects of the technology. A key advantage is vertical take off and landing (VTOL) of the flying rotor with the help of the ground rotor. For this purpose the generator, which is connected to the ground rotor, acts as a motor to power the rotation of the launching Parotor. A possible VTOL configuration of the small-scale model described in Sect. 22.4.1 is shown in Fig. 22.20.

Fig. 22.20 Possible configuration of the small-scale system shown in Fig. 22.7 before vertical launch maneuver

As shown in Fig. 22.9, and also in the conceptual design example discussed in Sect. 22.6.5, the outer diameter of the flying rotor can exceed the diameter of the ground rotor to some degree. It is not a problem in the case of the implementation of a rigid or semi-rigid [11] flying rotor. But in the case of the implementation of a flexible rotor, the diameter of the Parotor should not exceed the diameter of the ground rotor.

If there is no or very low wind the generator of the ground rotor is operated as a motor to keep the flying rotor airborne in a helicopter mode. The winches are also suitable to assure a fast landing in hazardous whether conditions. The envisaged emergency strategy for urgent depower uses a central depower line as illustrated in Fig. 22.5(c). The peripheral tethers are detached from the Parotor which is only kept by the central rope. Thus the Parotor turns around, losing its lift and drag, coming down towards the central station. In case of implementation of the second mode of generation, as described in Sect. 22.3.3, the suspension lines are also detached.

In case of failure of the electrical system and/or in case of rupturing of one or more tethers, the Parotor can be held by the central rope. The Parotor can also be held by the suspension lines (Figs. 22.6 and 22.5) if the second mode of generation is implemented as described in Sect. 22.3.3.

The wind velocity can vary significantly over the swept area of a huge flying rotor. A flexible rotor could employ active deformation of its blades to change their aerodynamic characteristics [12] and to adjust to varying wind conditions.

The RRP system follows the topology model of a single large rotary kite in steady-state rotation, anchored to the ground or sea surface by tethers [7, 30]. Thanks to its uniform motion a huge flying rotor is more easily recognized by other users of the airspace than a farm of smaller units with wings moving in multiple directions. Small wind turbines carrying lights are launched then move along the peripheral tethers. Then they are fixed at a desired height. They provide needed visibility markings.

An implementation of superimposed rotors is also studied. According to some observations [21, 24] there are possible interesting aerodynamic features increasing the efficiency of each rotor from a stack with regard to an identical but single rotor. A phase lag angle of a rotor with the nearby rotor can increase the transmission with relatively longer peripheral tethers. The rotors act then as “ring torque” [24].

22.8 Conclusions

In this chapter we have presented a rotary ring kite which uses a revolving tether system to transfer the generated aerodynamic torque to a ground rotor which is connected to a generator. To analyze this novel concept we have developed a kinematic model of the tether system and a numerical procedure to determine an approximate solution for steady-state rotation. This operational mode is characterized by minimal periodic compensation motions of the flying rotor. To realize this mode the flying rotor has to have specific aerodynamic characteristics and a specific inclination with

respect to the flow, also the length of the tethers has to be adjusted continuously with the rotation of the system.

The analysis has further revealed that the power transmission is an interplay between three periodically varying terms of equal magnitude: the power generated by the ring kite, the shaft power available at the ground and the net reeling power of the interconnected winch modules. For an ideal lossless system the net reeling power vanishes over an entire revolution and the transmission efficiency is 100%. In reality, however, energy conversion losses in the winch modules will reduce the transmission efficiency significantly. A possible solution to reduce these losses would be a mechanical interconnection, using electrical machines only to provide a differential reeling power.

We have also analyzed a secondary mode of energy conversion which is based on the selective unloading of the tethers during reel in. This is realized by periodically shifting the tensile load to additional suspension lines, with the theoretical result of a positive net reeling power of the interconnected winch modules. However, because of the inevitable cyclical force imbalance the system will tumble and a steady-state of operation can not be achieved.

Experimental tests with a small-scale model of the Rotating Reel Parotor system have confirmed some of the theoretical findings. In place of electrical machines, which would allow for precise actuation of the tethers, this first physical demonstrator uses winch modules with rotational spring mechanisms. As consequence, the results of this experiment can hardly be used to assess the original concept.

The present study serves as a starting point for future investigations. The planned prototypes increase in logical scaling steps: 5 m rotor diameter and tip height, then 10 m as small-scale models; 25 m, 50 m and 100 m as intermediate-scale models along with a critical assessment of the market opportunities in remote locations; 500 m, 1 km and more as large-scale models harnessing high-altitude winds at utility scale. An essential part of this roadmap is the question about the scalability of the Parotor towards very large dimensions.

The Python source code of the analysis tools developed in the frame of this chapter is available from a public repository [28].

Acknowledgements The authors would like to thank Antonello Cherubini for his help with the mechanical analysis; Antoine Delon, for the geometrical and mathematical representations of the reference axis and kinematics; Ben Lerner for the reorganization of some elements; David Murray for proofreading.

References

1. Ahrens, U.: Wind-operated power generator. US Patent 8,096,763, Jan 2012
2. Ahrens, U., Pieper, B., Töpfer, C.: Combining Kites and Rail Technology into a Traction-Based Airborne Wind Energy Plant. In: Ahrens, U., Diehl, M., Schmehl, R. (eds.) Airborne Wind Energy, Green Energy and Technology, Chap. 25, pp. 437–441. Springer, Berlin Heidelberg (2013). doi: 10.1007/978-3-642-39965-7_25

3. Archer, C. L., Caldeira, K.: Global Assessment of High-Altitude Wind Power. Energies **2**(2), 307–319 (2009). doi: 10.3390/en20200307
4. Argatov, I., Silvennoinen, R.: Asymptotic modeling of unconstrained control of a tethered power kite moving along a given closed-loop spherical trajectory. Journal of Engineering Mathematics **72**(1), 187–203 (2012). doi: 10.1007/s10665-011-9475-3
5. Argatov, I., Rautakorpi, P., Silvennoinen, R.: Estimation of the mechanical energy output of the kite wind generator. Renewable Energy **34**(6), 1525–1532 (2009). doi: 10.1016/j.renene.2008.11.001
6. Argatov, I., Silvennoinen, R.: Energy conversion efficiency of the pumping kite wind generator. Renewable Energy **35**(5), 1052–1060 (2010). doi: 10.1016/j.renene.2009.09.006
7. Beaujean, J. M. E.: 500MW Wind Turbines. Windtech International, 11 Nov 2011. https://www.windtech-international.com/content/500mw-wind-turbines Accessed 21 July 2016
8. Benhaïem, P.: Eolienne aéroportée rotative. French Patent 3034473, Oct 2016
9. Benhaïem, P.: Land and Space used. In: Lütsch, G. (ed.). Book of Abstracts of the International Airborne Wind Energy Conference 2013, p. 59, Berlin, Germany, 10–11 Sept 2013. http://resolver.tudelft.nl/uuid:e3e8aaa4-8ae1-498a-82ce-fdc7a149963f
10. Benhaïem, P.: Rotating Reeling. In: Schmehl, R. (ed.). Book of Abstracts of the International Airborne Wind Energy Conference 2015, p. 100, Delft, The Netherlands, 15–16 June 2015. doi: 10.4233/uuid:7df59b79-2c6b-4e30-bd58-8454f493bb09. Poster available from: http://www.awec2015.com/images/posters/AWEC25_Benhaiem-poster.pdf
11. Breuer, J. C. M., Luchsinger, R. H.: Inflatable kites using the concept of Tensairity. Aerospace Science and Technology **14**(8), 557–563 (2010). doi: 10.1016/j.ast.2010.04.009
12. Breukels, J., Schmehl, R., Ockels, W.: Aeroelastic Simulation of Flexible Membrane Wings based on Multibody System Dynamics. In: Ahrens, U., Diehl, M., Schmehl, R. (eds.) Airborne Wind Energy, Green Energy and Technology, Chap. 16, pp. 287–305. Springer, Berlin Heidelberg (2013). doi: 10.1007/978-3-642-39965-7_16
13. Burton, T., Jenkins, N., Sharpe, D., Bossanyi, E.: Wind Energy Handbook. 2nd ed. John Wiley & Sons, Ltd, Chichester (2011). doi: 10.1002/9781119992714
14. Canale, M., Fagiano, L., Milanese, M.: Power kites for wind energy generation - fast predictive control of tethered airfoils. IEEE Control Systems Magazine **27**(6), 25–38 (2007). doi: 10.1109/MCS.2007.909465
15. Diehl, M., Horn, G., Zanon, M.: Multiple Wing Systems – an Alternative to Upscaling? In: Schmehl, R. (ed.). Book of Abstracts of the International Airborne Wind Energy Conference 2015, p. 96, Delft, The Netherlands, 15–16 June 2015. doi: 10.4233/uuid:7df59b79-2c6b-4e30-bd58-8454f493bb09. Presentation video recording available from: https://collegerama.tudelft.nl/Mediasite/Play/1065c6e340d84dc491c15da533ee1a671d
16. Duquette, M. M., Visser, K. D.: Numerical Implications of Solidity and Blade Number on Rotor Performance of Horizontal-Axis Wind Turbines. Journal of Solar Energy Engineering **125**, 425–432 (2003). doi: 10.1115/1.1629751
17. Fletcher, C. A. J., Roberts, B. W.: Electricity generation from jet-stream winds. Journal of Energy **3**(4), 241–249 (1979). doi: 10.2514/3.48003
18. Hodges, T.: Centrifugally Stiffened Rotor. NIA Task Order Number 6528 Final Report, National Institute of Aerospace, 1 June 2015, pp. 57–147. http://ntrs.nasa.gov/archive/nasa/casi.ntrs.nasa.gov/20160001625.pdf
19. Ippolito, M.: Kite wind energy collector. Patent WO2014199407 A1, Dec 2014
20. Loyd, M. L.: Crosswind kite power. Journal of Energy **4**(3), 106–111 (1980). doi: 10.2514/3.48021
21. Michel, D., Koyama, K., Krebs, M., Johns, M.: Build and test a three kilowatt prototype of a coaxial multi-rotor wind turbine. Independent Assessment Report CEC-500-2007-111, Dec 2007. http://www.energy.ca.gov/2007publications/CEC-500-2007-111/CEC-500-2007-111.PDF
22. Moore, M. D.: Eternal Flight as the Solution for X. Presented at the NIAC 2014 Symposium, Stanford University, Palo Alto, CA, USA, 4–6 Feb 2014. https://www.nasa.gov/sites/default/files/files/Moore_EternalFlight.pdf

23. Rancourt, D., Bolduc-Teasdale, F., Demers Bouchard, E., Anderson, M. J., Mavris, D. N.: Design space exploration of gyrocopter-type airborne wind turbines. Wind Energy **19**, 895–909 (2016). doi: 10.1002/we.1873
24. Read, R.: Opportunities and Progress in Open AWE Hardware. In: Schmehl, R. (ed.). Book of Abstracts of the International Airborne Wind Energy Conference 2015, pp. 118–120, Delft, The Netherlands, 15–16 June 2015. doi: 10.4233/uuid:7df59b79-2c6b-4e30-bd58-8454f493bb09. Poster available from: http://www.awec2015.com/images/posters/AWEC23_Read-poster.pdf
25. Roberts, B. W., Shepard, D. H., Caldeira, K., Cannon, M. E., Eccles, D. G., Grenier, A. J., Freidin, J. F.: Harnessing High-Altitude Wind Power. IEEE Transactions on Energy Conversion **22**(1), 136–144 (2007). doi: 10.1109/TEC.2006.889603
26. Rye, D. C., Blacker, J., Roberts, B. W.: The Stability of a Tethered Gyromill. AIAA-Paper 81-2569. In: Proceedings of the AIAA 2nd Terrestrial Energy Systems Conference, Colorado Springs, CO, USA, 1–3 Dec 1981. doi: 10.2514/6.1981-2569
27. Schmehl, R.: Large-scale power generation with kites. Journal of the Society of Aerospace Engineering Students VSV Leonardo da Vinci March, 21–22 (2012). http://resolver.tudelft.nl/uuid:84b37454-5790-4708-95ef-5bc2c60be790
28. Schmehl, R.: Parotor. https://github.com/rschmehl/parotor. Accessed 25 Oct 2016
29. Selfridge, J. M., Tao, G.: Centrifugally Stiffened Rotor: A Complete Derivation and Simulation of the Inner Loop Controller. AIAA-Paper 2015-0073. In: Proceedings of the AIAA Guidance, Navigation, and Control Conference (AIAA SciTech), Kissimmee, FL, USA, 5–9 Jan 2015. doi: 10.2514/6.2015-0073
30. Snieckus, D.: Giant airborne 'power station' could blow rivals out of the water. Recharge News, 6 Mar 2012. http://www.rechargenews.com/news/technology/article1295509.ece Accessed 21 July 2016
31. Williams, P., Lansdorp, B., Ruiterkamp, R., Ockels, W.: Modeling, Simulation, and Testing of Surf Kites for Power Generation. AIAA Paper 2008-6693. In: Proceedings of the AIAA Modeling and Simulation Technologies Conference and Exhibit, Honolulu, HI, USA, 18–21 Aug 2008. doi: 10.2514/6.2008-6693